A&A, 698, A136 (2025)
https://doi.org/10.1051/0004-6361/202451124
© The Authors 2025

Astronomy & Astrophysics

Orbits of very distant asteroid satellites[⋆]

K. Minker[1,⋆⋆], B. Carry[1], F. Vachier[2], P. Scheirich[3], P. Pravec[3], T. Müller[4], A. Moór[5], C. Arcidiacono[6], A. Conrad[7], C. Veillet[7], S. A. Jacobson[8], M. Marsset[9], W. J. Merline[10], P. Tamblyn[10], M. E. Brown[11], D. Pray[12], R. Montaigut[13], A. Leroy[13], C. Gillier[13], P. Kušnirák[3], K. Hornoch[3], M. Husárik[14], V. Benishek[15], W. Cooney[16], J. Gross[16,†], D. Terrell[16,10], E. Jehin[17], J. Világi[18], Š. Gajdoš [19], V. Chiorny[20], B. Christmann[21], J. Brinsfield[22], C. Dumas[23], B. L. Enke[10], D. D. Durda[10], J. C. Christou[7,24], W. M. Grundy[25], L. M. Close[26], and S. B. Porter[10]

(Affiliations can be found after the references)

Received 14 June 2024 / Accepted 18 March 2025

ABSTRACT

Context. The very wide binary asteroid (VWBA) population is a small subset of the population of known binary and multiple asteroids made of systems with very widely orbiting satellites and long orbital periods, on the order of tens to hundreds of days. The origin of these systems is debatable, and most members of this population are poorly characterized.
Aims. We aim to develop orbital solutions for some members of the VWBA population, allowing us to constrain possible formation pathways for this unusual population.
Methods. We compiled all available high-angular-resolution imaging archival data of VWBA systems from large ground- and space-based telescopes. We measured the astrometric positions of the satellite relative to the primary at each epoch and analyzed the dynamics of the satellites using the Genoid genetic algorithm. Additionally, we used a NEATM thermal model to estimate the diameters of two systems, and we modeled the orbit of Litva's inner satellite using photometric light curve observations.
Results. We determine the effective diameters of binary systems (17246) Christophedumas and (22899) Alconrad to be 4.7 ± 0.4 km and 5.2 ± 0.3 km, respectively. We determine new orbital solutions for five systems, (379) Huenna, (2577) Litva, (3548) Eurybates, (4674) Pauling, and (22899) Alconrad. We find a significantly eccentric ($e = 0.30$) best-fit orbital solution for the outer satellite of (2577) Litva, moderately eccentric ($e = 0.13$) solutions for (22899) Alconrad, and a nearly circular solution for (4674) Pauling ($e = 0.04$). We also confirm previously reported orbital solutions for (379) Huenna and (3548) Eurybates.
Conclusions. It is unlikely that BYORP expansion could be solely responsible for the formation of VWBAs, as only (4674) Pauling matches the necessary requirements for active BYORP expansion. It is possible that the satellites of these systems were formed through YORP spin-up and then later scattered onto very wide orbits. Additionally, we find that some members of the population are unlikely to have formed satellites through YORP spin-up, and a collisional formation history is favored. In particular, this applies to VWBAs within large dynamical families, such as (22899) Alconrad and (2577) Litva, or large VWBA systems such as (379) Huenna and NASA's Lucy mission target (3548) Eurybates.

Key words. minor planets, asteroids: individual: (379) Huenna – minor planets, asteroids: individual: (2577) Litva – minor planets, asteroids: individual: (3749) Balam – minor planets, asteroids: individual: (4674) Pauling – minor planets, asteroids: individual: (22899) Alconrad – minor planets, asteroids: individual: (17246) Christophedumas

1. Introduction

There exists a small population of very wide binary asteroids (VWBAs) - binary or multiple systems with a satellite orbiting on a very distant orbit, with typical orbital periods over 50 days, and a semimajor axis that is typically >10% of the system's Hill radius (r_H). Most members of this class were discovered by direct imaging, through general surveys or targeted studies of asteroid families (Merline et al. 2002, 2003a,b, 2004; Tamblyn et al. 2004), and several potential members of this class have been predicted through light curve studies (Warner & Stephens 2019). In 2012, (2577) Litva became the first member of these predicted VWBA systems to be confirmed by direct imaging (Merline et al. 2013a,b). Analysis of asteroid observations in recent surveys (with PanSTARRS and ESA's Gaia, Ou et al. 2022; Liberato et al. 2024) and evidence in cratering records (Herrera et al. 2024) indicate that this population may be substantial, but this has yet to be confirmed by observations.

Wide binary systems have also been noted in the outer Solar System, categorized as ultrawide trans-Neptunian binaries (TNBs) (Parker et al. 2011). However, significant physical differences between the two populations (specifically, ultrawide TNBs must have nearly equal-sized components, but no such systems have been observed in the inner Solar System) indicate that they are influenced by distinct formation and dynamical processes. Nevertheless, both populations are defined by observational criteria (a minimum separation of 0.5″ at discovery for Parker et al. (2011), or the somewhat looser condition that the satellite must be resolvable from the primary for VWBAs) that could falsely dichotomize what is actually a smooth distribution.

Although only a few members of the VWBA population have been identified, this does not necessarily indicate that these systems are rare, as they are unusually difficult to observe. As the

---

[⋆] Based on observations made with ESO Telescopes at the La Silla Paranal Observatory under programme ID 074.C-0052, 71.C-0669, 072.C-0753.

[⋆⋆] Corresponding author: `kate.minker@oca.eu`

[†] Deceased.

possibility of detecting mutual eclipses by light curve indeed strongly decreases with mutual separation (Vavilov et al. 2022), the possibility of detecting mutual eclipses in VWBAs is nearly zero, and these systems can typically only be detected by direct imaging under very favorable observing geometries (Pravec et al. 2012b).

These systems should be easily detectable among near-Earth asteroids (NEAs) by radar, but such a population is yet to be identified. Fang & Margot (2012) illustrated that planetary encounters affect wider binary systems more than narrow binary systems, considering cases with semimajor axis to primary-diameter ratios of $2 < a/D_p < 8$, with increased chances of instability for distant satellites. The VWBA population members are significantly more widely separated than this, with typical ratios of $a/D_P \approx 50$–100. Extrapolating from the results of Fang & Margot (2012), any VWBAs that enter the NEA space would likely become unstable, and could be stripped of their satellites.

The origin of these systems is debated. Early predictions suggested that these objects could be escaping ejecta binaries (EEBs), formed through the mutual capture of ejecta particles during the catastrophic collision of a larger parent body (Durda et al. 2004). They could also form through Yarkovsky-O'Keefe-Radzievskii-Paddack (YORP, see, e.g., Vokrouhlický et al. 2015) spin-up and get excited to their very wide orbits through various mechanisms (Polishook et al. 2011; Jacobson et al. 2014).

Over the past decades, YORP spin-up has become the favored mechanism to explain the formation of satellites of small asteroids (Walsh et al. 2008). Satellites formed through this mechanism are easily identified as this population exhibits obvious signatures: rapid primary spin periods <4 h, a spin axis nearly perpendicular to the system's heliocentric orbital plane, a secondary-to-primary diameter ratio of $D_s/D_p \approx 0.3$, a system semimajor axis at ≈ 1.5–$2D_p$ (although some may be slightly more distant), and a preference for silicate compositions (Margot et al. 2015; Minker & Carry 2023). This mechanism is only effective for small (<10 km) systems, and is expected to be responsible for the formation of most small binary asteroid systems. While many systems show all of these characteristic signatures, others present only a fraction of these qualities. Most individual binary systems are not studied in detail, and a rapidly rotating primary for the system is often thought to be synonymous with YORP formation. This is likely an oversimplification, as an asteroid that has already acquired a satellite through another mechanism could still be susceptible to YORP spin-up of the primary. Although the typical YORP binary system has been studied in detail (Walsh et al. 2008; Pravec et al. 2010; Jacobson & Scheeres 2011), studies of population end members are typically less developed (Agrusa et al. 2024).

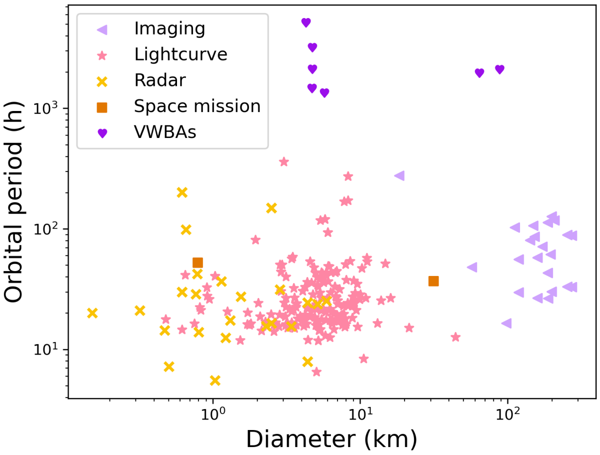

Fig. 1. Known binary asteroid systems, color- and symbol-coded by discovery method. Observational biases are clearly visible (for example, the populations of satellites discovered by imaging and light curves have no overlap), suggesting that gaps in the distribution (for example, in systems with $D_p \approx 50$ km or those with very long orbital periods) may simply be observational biases, not real attributes of the population. Systems discovered by stellar occultations are not shown, as the orbital periods are poorly constrained. Only systems with formal diameter estimates are included. As a result of this, systems with diameters <1 km are underrepresented.

The recent flyby on November 1, 2023 by NASA's Lucy mission (Levison et al. 2021, 2024) of the main-belt asteroid (152830) Dinkinesh revealed the presence of a previously undetected satellite, which was itself a contact binary. Such a system had never been observed previously, and this serves as a reminder that the currently observed population may not be representative of the true population of binary asteroids. Population end members and unique systems, such as (5457) Queen's and (243) Ida, are often discovered by unusual observational techniques (e.g., occultations, spacecraft flybys, see Manek et al. 2023; Chapman et al. 1995). Both of these systems fall in the poorly populated intermediate size range of $D_p \approx 20$–40 km (Figure 1). This suggests that there is more than meets the eye to the overall distribution of binary dynamics, and by extension the origins of these systems. Ill-studied portions of this dynamical space (for example, those with diameters between 10 and 100 km) could be crucial to deepening our understanding of binary asteroid formation, thereby expanding our view of ongoing dynamical processes affecting Solar System small bodies.

In this work, we present the first orbital solutions for three members of this group, (2577) Litva, (4674) Pauling, and (22899) Alconrad. We also report updates and confirmations on existing orbital solutions for (379) Huenna and (3548) Eurybates. We summarize the properties of these targets in Table 1, some of which were extracted from `SsODNet`[1] (Berthier et al. 2023).

The manuscript is organized as follows. In Sect. 2, we present the observational datasets used in this study, alongside our data reduction techniques, and describe in Sect. 3 the orbit determination techniques and the parameters used in the orbital solutions. We determine the physical properties of several of the targets in Sect. 4. The orbital solutions are presented in Sect. 5; and in Sect. 6 we discuss the implications of the presented results on the formation history of VWBAs.

2. Observational dataset

We have identified eight VWBAs for which imaging data were available: (379) Huenna, (1509) Esclangona, (2577) Litva, (3548) Eurybates, (3749) Balam, (4674) Pauling, (17246) Christophedumas, and (22899) Alconrad. For both Huenna and Eurybates, orbital solutions were recently published by Vachier et al. (2022) and Brown et al. (2021); Noll et al. (2023). We present here a minor update to the orbital solution for Huenna from that Vachier et al. (2022) containing an additional epoch of observations, and a solution derived from the astrometry presented in Brown et al. (2021) when discussing Eurybates.

---

[1] `https://ssp.imcce.fr/forms/ssocard`

Table 1. Basic parameters of known VWBA systems, from the literature.

Number	Name	Tax.	D_{eff} (km)	σ_D	P (h)	Dyn.	Family
379	Huenna	C$^{(1)}$	87.6$^{(2)}$	1.9	14.14$^{(8)}$	Outer MB	Themis
1509	Esclangona	S$^{(1)}$	9.5$^{(2)}$	0.6	3.25285$^{(9)}$	Hungaria	
2577	Litva	S$^{(1)}$	4.2$^{(2)}$	0.4	2.8129$^{(7)}$	Mars-Crosser	Hungaria
3548	Eurybates	P$^{(1)}$	63.8$^{(3)}$	0.4	8.73$^{(10)}$	Trojan	Eurybates
3749	Balam	S$^{(1)}$	4.7$^{(4)}$	0.2	2.804917$^{(11)}$	Inner MB	Flora
4674	Pauling	S$^{(1)}$	4.7$^{(5)}$	0.1	2.5313$^{(12)}$	Hungaria	
17246	Christophedumas	S$^{(6)}$	4.7$^{(7)}$	0.4	$>10^{(13)}$	Outer MB	Koronis
22899	Alconrad		5.2$^{(7)}$	0.3	4.03$^{(13)}$	Outer MB	Koronis

Notes. Listed are the asteroid name and number, taxonomic type ('Tax.'), effective diameter of the system ('D_{eff}', based off of an equal-volume sphere, except for Eurybates, where it is areal equivalent), uncertainty on the diameter (σ_D), rotation period ('P'), Dynamical class ('Dyn.'), and Family. The uncertainties on the diameter estimates are formal in most cases, and may be subject to additional systematic errors. References are as follows: (1)Mahlke et al. (2022), (2)Berthier et al. (2023) (3)Mottola et al. (2023b), (4)Masiero et al. (2011), (5)Myhrvold et al. (2022), (6)Sergeyev & Carry (2021), (7)This work, (8)Warner (2010), (9)Warner et al. (2009), (10)Stephens & Warner (2021), (11)Polishook & Aharonson (2020), (12)Warner (2011b), (13)Polishook et al. (2011).

2.1. Direct imaging of VWBA systems

To maximize the dataset, in terms of the number of both objects and observations per system, we have searched the archives of all large (8m-class) ground-based telescopes equipped with adaptive-optics cameras as well as the Hubble Space Telescope (HST), for observations of VWBAs. We found images of these systems in the archives of the HST, the European Southern Observatory (ESO) Very Large Telescope (VLT), Keck, and Large Binocular Telescope (LBT) observatories. Many of these observations are from observing programs led by authors of this study. Images taken at the ESO VLT used the Nasmyth Adaptive Optics System (NAOS) – Near-Infrared Imager and Spectrograph (CONICA) (NACO) instrument (Lenzen et al. 2003; Rousset et al. 2003), those from Keck were acquired with the NIRC2 instrument (van Dam et al. 2004), observations at LBT used the PISCES instrument[2], and the HST images were obtained with the High Resolution Channel (HRC) of the Advanced Camera for Surveys (ACS) instrument (Ryon & Stark 2023). The observing programs of these observations can be found under the following Program IDs; from ESO: 074.C-0052 (Principal investigator (PI): Marchis), 71.C-0669 (PI: Merline), 072.C-0753 (PI: Merline); from the W. M. Keck Observatory: N086N2 (PI: Merline), K296N2L (PI: Armandroff), N255N2L (PI: Merline), A283N2L (PI: Merline), N131N2L (PI: Porter), C232 (PI: Brown), as well as several instances of observations conducted on engineering time; and finally from the Hubble Space Telescope: 10165 and 9747 (PI: Merline). Some of these observations have been previously published with or without reports of satellite astrometry (see, for example, Merline et al. 2002, 2003a,b, 2004, 2013b; Tamblyn et al. 2004; Marchis et al. 2008).

All ground-based images were processed using standard image calibration techniques, including dark subtraction, flat-fielding, and the identification of dead and hot pixels, as well as halo-reduction algorithms to maximize the detectability of the satellite (Carry et al. 2008; Pajuelo et al. 2018). The astrometry of the satellite on each image was measured by fitting a 2D Gaussian profile. Examples of processed images can be found in Figure 2. In the case of (379) Huenna, most positions used here are duplicated from Vachier et al. (2022), which applied the same methodology.

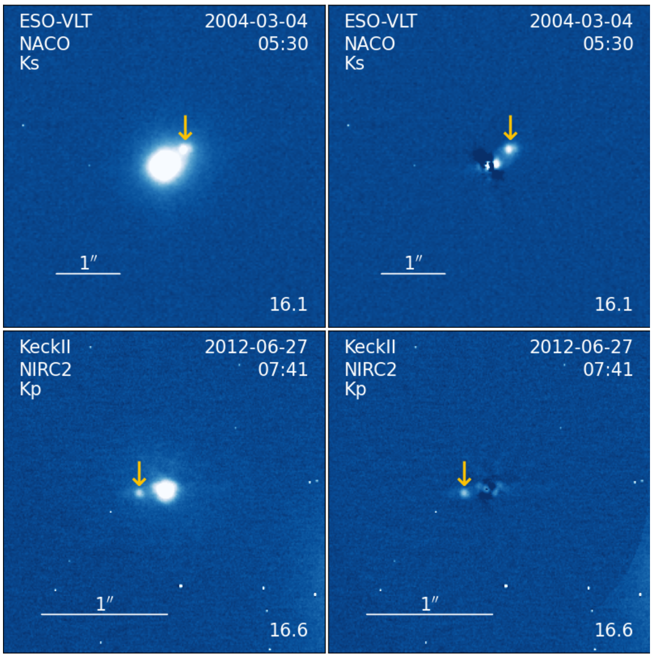

Fig. 2. Example of ground-based images for (4674) Pauling (top) and (2577) Litva (bottom). The two columns present the images before (left) and after (right) the application of halo-subtraction algorithm (see text). The arrows indicate the position of the satellite. The instrument and filter are indicated in the upper left corner of each image, the time of observation in the upper right corner, and the apparent magnitude in the lower right corner.

The processing and astrometry of images acquired with the HST were performed using DOLPHOT (Dolphin 2000, 2016). Pre-computed ACS PSFs were used to fit the astrometric positions of the primary and satellite in each image, one high-quality image was used per epoch. Only two systems were observed in this way: (17246) Christophedumas and (22899) Alconrad. We had a positive detection of the satellite in all but one epoch, resulting in the four and five positive detections for Christophedumas and Alconrad, respectively. Examples images can be found in Figure 3, and a detailed description of the observational epochs, images used, and astrometric positions reported can be found in Appendix A.

---

[2] `http://hdl.handle.net/20.500.12386/33745`

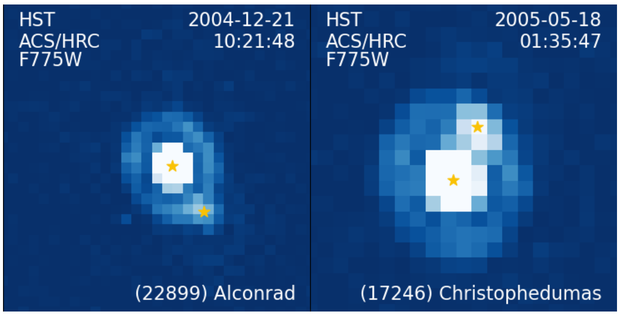

Fig. 3. Example of images of (22899) Alconrad (left) and (17246) Christophedumas (right) imaged by the HST. The measured positions of the primary and satellite are marked with yellow stars. The satellite position overlaps an Airy ring from the primary PSF in both images.

Unfortunately, we found (1509) Esclangona and (3749) Balam to have insufficient datasets for meaningful orbit determination. In the case of Esclangona, the satellite was resolved on only three dates, spread over nine years. This very low temporal-density dataset is not suitable for orbit determination. In the case of Balam, the present dataset is significantly reduced from previous studies (Marchis et al. 2008; Vachier et al. 2012). A known field-orientation issue with Gemini/Hokupa'a[3] prohibits the use of the discovery data of Balam's satellite (Merline et al. 2002). Although the satellite is clearly resolved in these images, the absence of a reliable field-orientation makes them unsuitable for orbital modeling. The dataset for Balam is further reduced as we were not able to find the satellite at the July 2003 and November 2004 epochs, reported in previous studies (Marchis et al. 2008; Vachier et al. 2012). Although we are unsure of the specific image processing techniques used to obtain the position of the satellite in these images, the conspicuous lack of reported satellite magnitudes on these dates combined with the fact that the reported separations on these dates are extremely small suggests that the reported positions were likely approximative. It is possible that the satellite was very close to the primary during these epochs, making it impossible to resolve the system. Since no precise satellite positions can be measured from these images, we exclude them from our dataset. We also found the dataset for (17246) Christophedumas to be insufficient to produce a robust orbital solution (see Section 5.6 for further information). We report the relative astrometry and photometry of all satellites in Appendix A.

2.2. Optical light curves

Two objects in our sample of VWBAs, (2577) Litva and (3749) Balam are triple systems and possess a closely-orbiting satellite in addition to their very wide satellite. For (2577) Litva, we constructed a model of the closely-orbiting satellite in addition to the very wide satellite in order to fully characterize the system. This was not replicated for Balam, as the orbit of the outer satellite is poorly constrained. In this work, we utilized the high-quality photometric observations of Litva that were taken in its four apparitions of 2009, 2010, 2012, and 2018. The observations taken in the first two of the four years were published in Pravec et al. (2012b). In 2012, it was observed from April 16 to June 19, from the following observatories: Skalnaté Pleso (with a 0.61-m telescope on 10 nights), Ondřejov (0.65-m, 7 nights), Via Capote (0.36-m, 4 nights), Sonoita Research Observatory (0.5-m, 4 nights), La Silla-TRAPPIST (0.6-m, 4 nights, Jehin et al. 2011), Modra (0.60-m, 2 nights), and Kharkiv (0.70-m, 2 nights). In 2018, it was observed from September 3 to 16, from following observatories: Sugarloaf Mountain (0.50-m, 4 nights), OPERA (0.20-m, 3 nights), Soucieu-en-Jarrest (0.20-m, 3 nights), and Sopot (0.35-m, 1 night). The observations from the individual stations were processed using the standard techniques (bias, dark and flat field corrections) and photometrically reduced with the aperture photometry method using specific software packages utilized at the individual observatories. The observational and reduction techniques utilized at the individual observatories were described in Pravec et al. (2012b, 2014, 2016, 2019); Montaigut et al. (2019) and in Benishek (2019). Generally, they were high-quality data with the RMS residuals (in the binary light curve decomposition; see below) of 0.013 and 0.015 mag in 2012 and 2018, respectively. The data taken with the 0.65-m telescope at Ondřejov on the 7 nights in 2012 were absolutely calibrated in the Cousins R system with the Landolt (1992) standards with the absolute calibration errors of 0.01 mag. The data from the other observatories were taken as relative or they were calibrated in different photometric systems with a lower internal consistency and we used them as relative, taking the zero points of the magnitude scales on the individual nights as free parameters and adjusting them for the best fit in the light curve decompositions below.

2.3. Mid-infrared photometry

Two of the systems here, (17246) Christophedumas and (22899) Alconrad, had no published diameter estimate. We thus searched for mid-infrared data to constrain their diameter and albedo (discussed in Sect. 4). We found that both systems were observed during the course of the NASA Wide-field Infrared Survey Explorer (WISE) survey (Wright et al. 2010). They were also the target of a NASA Spitzer program [P. Tamblyn, PID:20538] with the Infrared Array Camera (IRAC) instrument (Fazio et al. 2004).

The Spitzer observations were carried out using all four IRAC bands at 3.6, 4.5, 5.8, and 8.0 μm. Christophedumas was measured on August 22, 2005, while the observation of Alconrad was made on December 27, 2005. To extract the flux densities of the asteroids, we used aperture photometry on the individual corrected basic calibrated data (CBCD) images produced by the IRAC pipeline and downloaded from the Spitzer Heritage Archive (AORKEY: 14818304 and 14818560 for Christophedumas and Alconrad, respectively). The aperture radius was set to 2 pixels (~2.4″), and the sky level was estimated by computing a robust average in a radial annulus from 2 to 6 pixels. We applied aperture correction using the appropriate factors from the IRAC Instrument Handbook v4.0[4] and pixel phase correction employing the `irac_aphot_corr` task[5] developed by the Spitzer Science Center. To derive the final photometry and the uncertainties, we computed the mean and the error of the mean of the individual flux density measurements using an outlier resistant method. All these data are summarized in Appendix B, where the total uncertainties – the quadratic sums of the measurement errors and the calibration uncertainties (IRAC Instrument Handbook) – are also given. For both systems,

---

[3] `https://www.gemini.edu/sciops/instruments/uhaos/uhaosIndex.html`

[4] `https://irsa.ipac.caltech.edu/data/SPITZER/docs/irac/iracinstrumenthandbook/`

[5] `https://irsa.ipac.caltech.edu/data/SPITZER/docs/dataanalysistools/tools/contributed/irac/iracaphotcorr/`

model calculations show that the IRAC1 and IRAC2 bands contain significant contributions of reflected sunlight, so we focused on the IRAC3 and IRAC4 bands. The in-band fluxes were color-corrected to obtain monochromatic flux densities. Ultimately, diameters of 4.7 ± 0.4 km and 5.2 ± 0.3 km were determined using the process described in Section 4.1 for Christophedumas and Alconrad, respectively. A description of the diameter estimates for all systems considered in this study can be found in Table 1.

3. Orbit determination

We determined the best-fit orbital solutions for the binary systems with the `Genoid` algorithm (Vachier et al. 2012). `Genoid` is a genetic algorithm that searches for the dynamical parameters of the orbital motion in a binary or multiple system through successive generations of randomly matched solutions. The first generation of solutions is drawn randomly over a large range of values for each parameter (mass of the components, semi-major axis, etc.). An ephemeris for each observing date is then computed using Eproc (Berthier 1998), the computation library behind IMCCE online ephemerides (Berthier et al. 2006, 2016; Carry & Berthier 2018). A fitness function based on χ^2 is minimized during the process to determine the solution that shows the lowest residuals between the observed and computed positions (hereafter “o–c”). The high number of trial solutions (from 300 000–2 000 000 depending on the complexity of the system) combined with the numerous successive generations (1000) ensures both a wide exploration of the parameter space and convergence toward the global minimum of residuals. A complete description of the method can be found in Vachier et al. (2012), and other applications of this algorithm can be found in, for example, Berthier et al. (2014), Pajuelo et al. (2018), Carry et al. (2019, 2021), Yang et al. (2020), and Vachier et al. (2022). Uncertainties on variable parameters are statistical, not formal, and represent the range of values present in solutions where the RMS residuals are below the average 1 σ threshold. Since most orbits calculated with `Genoid` have RMS residuals significantly below this threshold, this may result in the overestimation of these statistical uncertainties.

Due to the limited size of our datasets, for most systems we restrict the solutions to simple Keplerian orbits, and all higher order terms (external perturbation of the Sun and planets, influences due to the nonspherical nature of the systems' primaries) have been neglected. In other terms, the dynamical system reduces to a restricted two-body problem. However, we wish to note that the very wide nature of these orbits implies that the Sun and planets likely have a substantial influence on the long-term orbital dynamics, and it will likely be necessary to fit long-term orbital solutions incorporating future observations. In the case of (379) Huenna and (3548) Eurybates, the dataset is much larger, so we have included these perturbations, as was previously described by Vachier et al. (2022). The mass of the satellite is also non-negligible, such that the center of mass of the system is likely outside of the primary. However, the one-pixel uncertainties on the position of the primary encompass the anticipated location of the center of mass (assuming equal density and albedo of all components), and as such the center of mass can be approximated as the photocenter of the primary for the present limited dataset. The masses reported in Section 5 represent the total system mass, assuming a Keplerian orbit. Similarly, in the case of the triple systems, the inner satellite may cause a discrepancy between the photocenters' and the systems' center of mass, but once again we estimate this discrepancy to be negligible, and therefore approximate the inner two components of the system as one central object. The results of these orbital fits can be found in Section 5.

4. Physical models

4.1. Diameter estimates

One object from our sample, (17246) Christophedumas, does not have a diameter estimate reported in the literature, and that of (22899) Alconrad has only one reported estimate (Masiero et al. 2011) that does not include all available data. We have derived diameter and albedo estimates for these two asteroids as is described in the following, using thermal observations described in Section 2.3.

4.1.1. (17246) Christophedumas

We applied a simple thermal model for NEAs (NEATM, Harris 1998) to the derived fluxes presented in Table B.1. The NEATM analysis of the IRAC data returns a beaming parameter of 1.165, a diameter of 4.8 ± 0.1 km and a geometric V-band albedo of $p_V = 0.21 \pm 0.04$ when assuming $H_V = 13.93 \pm 0.2$. For the H_V the ATLAS orange-band H_o from Mahlke et al. (2021) was used, and translated into H_V by the method of Shevchenko et al. (2022, & private communication) (see also footnote 9 in Müller et al. 2023).

This diameter estimate represents the effective diameter of the entire binary systems ($D_{\rm eff}$) and uncertainties are formal, although these estimates maybe be subject to additional systematic uncertainties. The best NEATM solution for the WISE data is found for a beaming parameter of 1.22, a size of 5.01 ± 0.5 km and a geometric V-band albedo of 0.19 ± 0.04. The IRAC and WISE solutions are perfectly compatible, in beaming parameter and size-albedo solution. However, the IRAC-derived size and albedo has a higher accuracy. Assuming the 0.15 mag lower limit on the light curve amplitude (Polishook et al. 2011), it could also be that the measurements by IRAC in 2005 and WISE in 2010 have seen the system at different rotational phases and also under a different aspect angle. Only a high quality spin-shape solution for the system would make it possible to constrain a single size-albedo solution. As the IRAC (phase angle α of –21°) and WISE data (α=+21 deg) are taken before and after opposition, respectively, a reliable spin-shape solution would also make it possible to constrain the object's thermal properties. A first attempt using a thermophysical model (TPM, Lagerros 1996a,b, 1997, 1998; Müller & Lagerros 1998) assuming the 10h lower limit on the rotation period (Polishook et al. 2011), and a spin-pole perpendicular to the ecliptic plane gave a radiometric size (for the combined WISE & IRAC dataset) of 4.7 ± 0.4 km (of an equal-volume sphere), a geometric V-band albedo p_V of 0.22 ± 0.04 and a strong indication for a thermal inertia in the range 4–50 J m^{-2} s$^{-0.5}$ K^{-1}. Considering a diameter ratio of 0.34 between the primary and the secondary, this becomes diameters of 4.4 km and 1.5 km for the two components of the system. An illustration of the χ^2 curves from the TPM fit can be found in Figure C.1.

4.1.2. (22899) Alconrad

The NEATM analysis gave a beaming parameter of 1.15, a size of 4.9 ± 0.2 km and a geometric V-band albedo of 0.26 ± 0.04 (assuming $H_V = 13.65 \pm 0.2$, derived following the same methods as are described in Section 4.1.1 from $H_o = 13.33$ from Mahlke et al. 2021). Masiero et al. (2011) used 11 WISE-W3 and 7 W4 detections to derive a NEATM-based size and albedo solution with D=5.68 ±0.47 km, $p_V = 0.18 \pm 0.03$ taking an H-mag of 13.70 and a fixed beaming parameter of 1.30 ± 0.16. MPC archive lists additional detections, 13 in total (observatory code C51).

All W3 and W4 detections happened in the time period between 12:23 on March 10, 2010 and 15:22 on March 11 2010 (mid-time: 02:00 on March 11 2010, 2455266.58333: r=2.91372 au, δ=2.64959, α= +19.8). The W3 and W4 multiband detections show some scatter in flux but no W3-W4 synchronized variation as one would expect for a shape-driven thermal light curve. Therefore, we calculated the weighted average of the good-quality (flag '0A') W3 and the best-quality W4 points (after applying color correction factors of 0.94 and 0.98 in W3 and W4, respectively) (Szakáts et al. 2020). The results are: 6.09 ± 0.58 mJy at 11.1 micron, and 16.96 ± 1.14 mJy at 22.64 micron. A NEATM calculation leads to a size of $D = 4.9 \pm 0.2$ km, geometric V-band albedo of $p_V = 0.25 \pm 0.05$ (using the $H_V = 13.65$, see above), and a best-fit beaming parameter $\eta = 1.05$. The IRAC and WISE solutions are compatible, in beaming parameter and size-albedo solution. However, the IRAC-derived size and albedo has a slightly higher accuracy. It should also be mentioned that the radiometric solution is related to the size of an equal-volume sphere for the combined binary system. As the light curve amplitude of the system is found to be between 0.14 and 0.19 mag (Polishook et al. 2011), it could also be that the measurements by IRAC in 2005 and WISE in 2010 have seen the system at different rotational phases and also under a different aspect angle. Only a high quality spin-shape solution for the system would make it possible to constrain a single size-albedo solution. The IRAC (α=+19.3°) and WISE data (α=+19.8°) are both taken after opposition, which makes a study of thermal properties more challenging.

A first attempt using a TPM with a 4.03 h rotation period (Polishook et al. 2011), and a spin-pole perpendicular to the orbital plane of the satellite $(\lambda, \beta)_{ECJ2000} = (330°, -54°)$, in other words, a retrograde sense of rotation, gave a radiometric size (for the combined WISE & IRAC dataset) of 5.2 ± 0.3, $p_V = 0.24 \pm 0.03$ and an indication for a thermal inertia between 30 and 100 J m^{-2} $s^{-0.5}$ K^{-1}. Notably, the 4.03 h spin period may be unreliable, as an alternative estimation of 5.02 h is reported by Waszczak et al. (2015). This TPM radiometric solution fits the data on an accepted level (reduced χ^2 close to 1.0), but it is closely connected to the retrograde sense of rotation of the primary derived from the satellite's orbit. When using a prograde sense of rotation with $(\lambda, \beta) = (330°, +54°)$ the radiometric solution changes dramatically: the reduced χ^2 (for the best TPM solution in comparison with the combined WISE and IRAC data) jumps to values above four which means that a prograde rotation of the primary body is not compatible with the available thermal measurements (see also χ^2 plot in the appendix, Figure C.1). However, also the retrograde TPM solution should be taken with care as it depends strongly on the assumed spin-pole and thermal properties. In addition, the best-fit thermal inertia (which determines the final radiometric size) might be affected by unknown shape effects. Such radiometric studies suffer therefore from errors in the model input parameters which are difficult to quantify.

4.2. Inner satellite of (2577) Litva

We constructed a model of the orbit of the inner moon of Litva using the technique of Scheirich & Pravec (2009), modified to allow for precession of the pericenter in the case when modeling the eccentric orbit (see below), that was further developed by Scheirich et al. (2015) and Scheirich et al. (2021). We outline the basic points of the method below, but we refer the reader to the above references for details of the technique.

The binary asteroid components were represented with a sphere (for the inner moon) and oblate ellipsoid (for the primary), orbiting each other on a circular orbit. We choose the circular orbit for simplicity, as the upper limit on the eccentricity is low (see below). The motion was assumed to be Keplerian. The spin axis of the primary was assumed to be normal to the mutual orbital plane of the components (i.e., we assumed the mutual orbit is in the equatorial plane of the primary). The shapes were approximated with 1016 and 252 triangular facets for the primary and the secondary, respectively. The components were assumed to have the same albedo and to be free of albedo features (see Kaasalainen & Torppa 2001, for discussion on why albedo features can be neglected). The brightness of the system as seen by the observer was computed as a sum of contributions from all visible facets using a ray-tracing code that checks which facets are occulted by or are in shadow from the other body. A combination of Lommel–Seeliger and Lambert scattering laws was used (see, e.g., Kaasalainen et al. 2002).

The photometric data were analyzed using the binary asteroid light curve decomposition method (Pravec et al. (2022), and references therein). There were present two rotational light curves in the data, one belonging to the primary and the other belonging to the outer satellite, with spin periods of 2.8129 and 5.6818 h, respectively (Pravec et al. 2016). Both rotational light curves were subtracted from the photometry data with the light curve decomposition technique and we obtained the orbital light curve component, showing mutual events (eclipses and/or occultations) between the primary and the inner satellite.

The solution for the parameters of the orbit of the inner satellite given in Table 4 was obtained by fitting our model to the orbital light curve component from the apparitions 2009, 2010, 2012 and 2018 simultaneously. To account for the presence of the third body, a total light flux scattered towards the observer was computed as $I_1 + I_2 + I_3$, where I_1 is the light flux from the ith body. We set $I_3/(I_1 + I_2) = 0.053$ (i.e., the square of the size ratio between the outer satellite and the combined light of the primary and inner satellite, see Sect. 5.2). The upper limit on the eccentricity was estimated by fitting the orbital light curve component from the best-covered apparition (2012) only. Examples of the orbital light curve component of the observed data together with a synthetic light curve for the nominal solution are presented in Fig. 4.

5. Orbit determination results

We present here the orbital solutions we found for the VWBAs. A brief overview of all of the systems can be found in Table 3, and additional details for each system are provided in the following subsections. Ephemeris for these satellites, and other `Genoid` orbital solutions, are publicly accessible online[6] through the LTE (previously known as IMCCE) Solar System portal (SSP).

5.1. (379) Huenna

The orbital solution for asteroid (379) Huenna presented here is a minor update to the Vachier et al. (2022) solution, yielding

---

[6] `https://ssp.imcce.fr/webservices/miriade/api/ephemsys/` Due to recent laboratory name changes, this url may change in coming years. Please contact K. Minker, B. Carry, or F. Vachier if you have trouble accessing ephemerides.

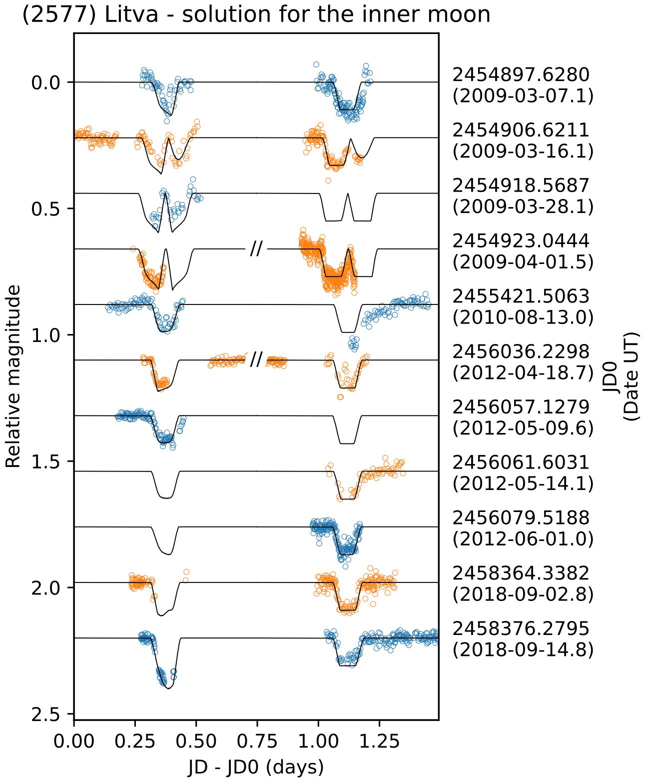

Fig. 4. Example of orbital (mutual event) light curves of the inner satellite of (2577) Litva observed in 2009, 2010, 2012 and 2018. The observed data with the rotational light curves of the primary and the outer satellite subtracted using the binary asteroid light curve decomposition method (Pravec et al. 2022, and reference therein) are marked as points. The solid curve represents the synthetic light curve for the nominal solution for the inner moon. The primary and secondary events are always shown on the left and right sides of the plots, respectively. In two cases where the secondary event was observed before the primary event, we present them in reverse order, separated by the // symbol and one orbital period (1.4946 day).

similar results with a significantly longer orbital baseline therefore validating the long term stability of the Vachier et al. (2022) solution. We find an orbital period of 80.2 d, a semimajor axis of 3489 km, and eccentricity of 0.28. New observations on 2021-11-18 (Keck/NIRC2, PID:C232, PI:Brown) extend the dataset by an additional seven years compared to Vachier et al. (2022), to a total of 18 years of observations. The changes in determined orbital elements are negligible given the uncertainties. Our new orbital solution, based on 42 observations spanning 6671 days, with a root mean square (RMS) of the residuals between the observed positions and those predicted of 5.45 mas only (≈0.5 px), can be seen in Table 2. The significantly nonzero eccentricity observed in Huenna's satellite is similar to some small VWBA systems, such as (2577) Litva (see below). We observe a non-negligible influence of solar perturbations. This orbital solution is stable enough to be used reliably for predicting stellar occultations of the satellite in the forthcoming years.

5.2. (2577) Litva

For this triple asteroid system, we present two orbital solutions: one for the inner satellite based on photometric light curve observations of the system (Sect. 2.2) and a second for the outer satellite based on direct measurements of satellite positions (Sect. 2.1). Both of these solutions are described in Table 4.

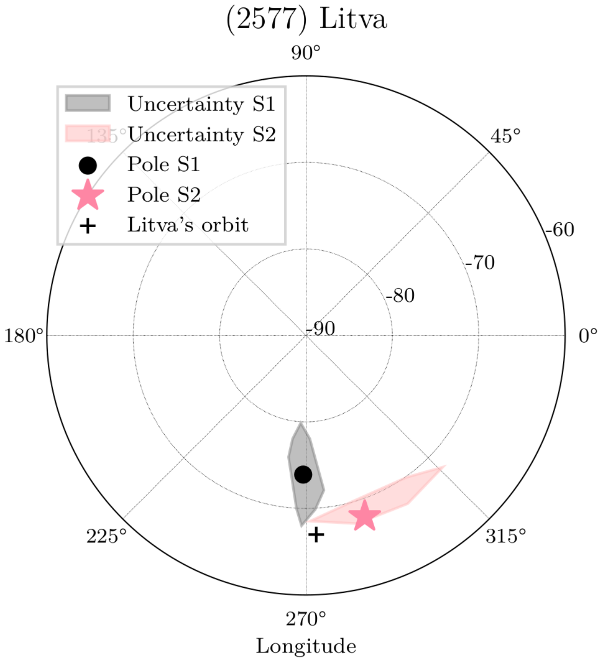

Fig. 5. Orbital poles of Litva's satellites with uncertainties. 3-sigma area of uncertainty of the orbital pole of Litva's inner satellite (S1) is represented in gray, and the 3-sigma area of uncertainty of the orbital pole of Litva's outer satellite (S2) in pink. The orbital pole of S1 is marked by a black circle, and the orbital pole of Litva's outer satellite S/2012 (2577) 1 (S2) is marked by a pink star. The orbital pole of Litva's heliocentric orbit is marked by a black cross.

The orbital solution for the inner satellite, based on a nine-year period of observations (2009–2018), is in general agreement with the previously published solution from Pravec et al. (2012b). We determine an orbital period of 35.87101 ± 0.00022 h, with uncertainties at the 3σ level. The solution that we present includes the known outer satellite of $D_s/d_c = 0.23$, where d_c is the quadratic sum of the diameters of the primary and the inner satellite (Appendix A).

The orbital solution derived here for Litva's outer satellite confirms the very long orbital period reported by Merline et al. (2013a), and we find good agreement between the periods (215 ± 37 against 214 days) and the semimajor axes (347 ± 44 km against 378) of the two solutions. This solutions encompasses the observations used for the preliminary study of the orbit at the time of discovery, with an additional epoch in 2004 providing a much longer temporal baseline (Table A.2). The orbit is notably eccentric ($e = 0.31$), which is uncommon among most asteroid satellites, but similar to that of the satellite of (379) Huenna (see above and Vachier et al. 2022). The positions of the satellite predicted by this orbital solution match the observed positions very well, with RMS residuals of 3.09 mas.

Our initial orbital solution for Litva, which used only the observations from 2012–2013, was degenerate, with two possible orbital-plane-orientations for the system. Ultimately, we were able to reject one solution by considering the orbital orientation of the inner satellite, under the assumption that the orbits of both satellites are not far from co-planar (as is the case for most triple systems, e.g., Brozović et al. 2011; Carry et al. 2021; Brož et al. 2021). However, a slight (10°) offset can be observed between the orbital axis of the two satellites (Fig. 5). We were then able to confirm this by comparison with the 2004 observation that provided a faint detection of the satellite close to the primary

Table 2. Orbital elements of the satellite of Huenna, expressed in EQJ2000, obtained with `Genoid`.

	(379) Huenna and S/2003 (379) 1	
Observing dataset		
Number of observations	42	
Time span (days)	6671	
RMS (mas)	5.45	
Orbital elements EQJ2000		
P (days)	80.21585	±0.01450
a (km)	3488.8	±48.4
e	0.283	±0.010
i (°)	151.1	±0.7
Ω (°)	204.4	±1.3
ω (°)	278.8	±1.5
t_p (JD)	2452930.95866	±0.30025
Derived parameters		
M ($\times10^{17}$ kg)	5.229	±0.218
λ_p, β_p (°)	161, –78	±4, 1
α_p, δ_p (°)	114, –61	±1, 1

Notes. Orbital period P, semimajor axis a, eccentricity e, inclination i, longitude of the ascending node Ω, argument of pericenter ω, time of pericenter t_p. The number of observations and RMS between predicted and observed positions are also provided. Finally, we report the mass of Huenna M_{Huenna}, the ecliptic J2000 coordinates of the orbital pole (λ_p, β_p), the equatorial J2000 coordinates of the orbital pole (α_p, δ_p). Uncertainties are given at the 1-σ level.

and an exceptionally good match to the preliminary ephemeris despite the eight year observational gap between the 2004 and 2012 observations. This point was included in the final orbital solution.

Photometric light curve observations of Litva indicate an axial ratio c/a of $0.67^{+0.33}_{-0.23}$ (3-sigma uncertainties). This suggests that Litva may be similarly oblate to other small, well studied binary systems, including (65803) Didymos (c/a = 0.72, Chabot et al. 2024) and (66391) Moshup (c/a = 0.86, Ostro et al. 2006). In the absence of an accurate shape model of Litva's primary, it is unclear whether Litva shares the elongated-ellipsoid shape common amongst larger binary systems (for example, (243) Ida, see the trend in Carry et al. 2021), or the top-shape common amongst NEA binaries (for example, (65803) Didymos). Development of an accurate shape model for Litva or any other VWBA systems could provide valuable clues to their formation (Zhang et al. 2022). However, the relatively low light curve amplitude of litva (0.17 mag) across multiple apparitions suggests that the system's primary is unlikely to be heavily elongated.

5.3. (3548) Eurybates

Eurybates, future rendezvous target of NASA's Lucy mission, is the only known VWBA system among the Jupiter Trojans. Previous solutions have been published by Brown et al. (2021) and Noll et al. (2023), with a minor disagreement (3σ) in eccentricity between the two. Here, we present an alternative solution calculated from the astrometry presented in Brown et al. (2021). The Noll et al. (2023) solution also contains additional HST observations from December 2021 (mistakenly reported as December 2022 in Noll et al. 2023), For consistency, we choose to only include the astrometric positions reported by Brown et al. (2021). We reproduce these positions in Table A.3, with minor corrections to astrometric sign errors and observation dates.

The results of our solution are presented in Table 6. We use a model that includes Keplerian motion and Solar tides, which produced results consistent with those of Brown et al. (2021) within 1σ uncertainties. The inclusion of Solar tides, which were included in the Noll solution but not the Brown solution, could explain the discrepancy between the Brown et al. (2021) and Noll et al. (2023) models. We note that the statistical uncertainties present by `Genoid` are often somewhat overestimated for certain parameters, and that our Solar-tide model matches slightly better with the tideless Brown model than the Solar-tide Noll model.

We also attempted a solution with fixed astrometric uncertainties for all points (as was done with HST solutions for Alconrad and Christophedumas), rather than the astrometric uncertainties presented by Brown et al. (2021). This presented a slightly better fit (RMS=6.38 mas vs. RMS=7.89 mas).

5.4. (3749) Balam

Balam is one of the most interesting known multiple asteroid systems, exhibiting a complex dynamical geometry involving one close satellite, one distant satellite, and one unbound (escaped) satellite, in the form of a pair (Pravec et al. 2019). Until this point, (3749) Balam has been the only small VWBA system for which an orbital solution has been published in the literature (Marchis et al. 2008), albeit the solution was heavily degenerate and numerous sets of parameters could fit the data equally well (see Vachier et al. 2012). However, as pointed out in Sect. 2, the field orientation of the earliest Gemini/Hokupa'a data is deemed unreliable. This significantly reduces the amount of available positions to 9 observations over only 17 days. As the orbital period could be over a factor of four longer than the time span of the observations, this extremely limited dataset prohibits the development of a meaningful orbital solution.

We note that eccentric solutions were slightly more favorable than strictly circular solutions (9.8 mas residuals vs 11.2 mas residuals), with reasonable solutions found for $0.2 < e < 0.8$. The lack of detection of the satellite in some images suggests that the satellite might be very close to the primary at this time, supporting this hypothesis. Notably, the prior orbital solutions presented significant degeneracies in key parameters (see Vachier et al. 2012) and large uncertainties, supporting our decision to exclude these observations.

5.5. (4674) Pauling

For (4674) Pauling, no previously-computed orbital solution can be found in the literature. Our solution fits the 14 observations with a RMS residual of 5.13 mas. The semimajor axis is found to be 310 ± 30 km, and the low eccentricity ($e = 0.04^{+0.08}_{-0.04}$) is compatible with a purely circular orbit. Assuming a primary diameter of 4.7 ± 0.1 km (Myhrvold et al. (2022), although diameters from mid-infrared radiometry may be affected by systematic errors of about 10%, Masiero et al. (2018)) and similar densities for the primary and satellite, we determine a density of 2.4 ± 0.7 g cm^{-3} for the system. The value is in line with density values reported for other small S-type asteroids (e.g., Carry 2012; Scheirich & Pravec 2022). A detailed description of the orbital solution can be found in Table 5.

5.6. (17246) Christophedumas

Here we present our orbital analysis for (17246) Christophedumas. Unfortunately, there is a high level of ambiguity in this

Table 3. Table of orbital properties calculated for VWBA systems.

Number	Name	a(km)	σ_a	e	σ_e	M_p(10^{14}kg)	σ_{M_p}	ρ	σ_ρ	D_s(km)
1509	Esclangona									1.4
2577	Litva	348	44	0.30	0.09	0.72	0.24	1.9	1.3	1
3749	Balam			>>0						1
4674	Pauling	310	30	0.035	0.08	1.33	0.36	2.4	0.7	1
22899	Alconrad	204	18	0.13	0.1	2.13	0.56	2.9	0.9	1.8
17246	Christophedumas	259	8	0.183	0.024	1.78	0.14	3.3	0.9	1.6
379	Huenna	3489	48	0.28	0.01	5230	220	1.5	0.1	3
3548	Eurybates	2350	40	0.13	0.03	1500	90	1.1	0.3	0.8

Notes. For (3548) Eurybates the satellite diameter is extracted from Noll et al. (2020). In the case of Balam and Litva, D_s refers to the outermost satellite.

Table 4. Orbital solutions for the two satellites of Litva, expressed in EQJ2000, obtained with `Genoid`, and by the methods described in Sections 2.2 and 5.2.

	(2577) Litva and S/2012 (2577) 1	
Observing dataset		
Number of observations	22	
Time span (days)	3522	
RMS (mas)	3.09	
Orbital elements EQJ2000		
P (days)	214.79901	±37.10072
a (km)	347.8	±43.6
e	0.302	±0.094
i (°)	172.9	±7.4
Ω (°)	87.3	±26.1
ω (°)	162.5	±36.5
t_p (JD)	2456105.35556	±12.06249
Derived parameters		
M ($\times 10^{13}$ kg)	7.227	±2.477
λ_p, β_p (°)	288, –66	±20, 3
α_p, δ_p (°)	357, –83	±26, 7
Λ (°)	11.5	±1.3
Inner satellite		
P_{orb} (hours)	35.87101	± 0.00022
P_{orb} (days)	1.4946254	± 0.000092
$a/D_{\rm eff}$	2.44	± 0.57
a (km)	10	±3
e	<0.07	
D_s/D_p	0.34	±0.02
c/a	0.67	+0.33 –0.23
λ_p, β_p (°)	269.0, –74	±7.3, 6

Notes. Please see Table 2 for a description of the listed parameters. Uncertainties are given at 1-σ for the outer satellite, and 3-σ for the inner satellite. $D_{\rm eff}$ represents the equivalent diameter of the Litva system, and the orbital inclination (Λ) with respect to the orbital plane of the inner satellite.

Table 5. Orbital elements of the satellite of Pauling, expressed in EQJ2000, obtained with `Genoid`; please see Table 2 for a description of the listed parameters.

	(4674) Pauling and S/2004 (4674) 1	
Observing dataset		
Number of observations	14	
Time span (days)	3055	
RMS (mas)	5.13	
Orbital elements EQJ2000		
P (days)	133.29069	±0.25397
a (km)	310.0	±29.9
e	0.035	$^{+0.080}_{-0.035}$
i (°)	161.2	±3.8
Ω (°)	132.9	±8.9
ω (°)	174.4	±50.1
t_p (JD)	2453118.40620	±17.68012
Derived parameters		
M ($\times 10^{14}$ kg)	1.329	±0.367
λ_p, β_p (°)	325, –73	±13, 3
α_p, δ_p (°)	43, –71	±9, 4

orbital solution, as such we were not able to achieve an orbital fit that is physically reasonable and also has an acceptable RMS. We were able to develop an extremely low-residual (0.23 mas RMS) orbital solution for the system. The physical parameters derived from this solution are, however, in contrast to our expectations. The orbital solution (in combination of the system diameter of 4.7 ± 0.4 km determined in section 4.1.1) indicates an extremely high-density primary, (6.6 ± 1.8 g.cm^{-3}), which poorly aligns with other members of the Koronis family (Petit et al. 1997), other VWBA systems (see Table 3), and the general asteroid population (Carry 2012; Vernazza et al. 2021). Furthermore, this orbital solution indicates that the satellite should be at a wider separation from the primary than any other epoch of observation during the 2005-07-04 non-detection. Since there are no obvious issues with image quality, it is suspicious that the satellite would not be resolvable at this time, given that it was successfully resolved at much smaller angular separations. Due to the algorithm used by `Genoid` to determine determine best-fitting parameters, inserting a "false" point with a very large uncertainty to represent the non-detection would heavily bias the results, and as such it is not possible to constrain the solutions in this way. Therefore, we discard this solution.

We were able to determine an alternate solution by restricting the mass of the system to only provide solutions with a physically reasonable ($\rho \lesssim 4$ g cm^{-3}) density. The orbital fit is

Table 6. Orbital elements of the satellite of Eurybates, expressed in EQJ2000, obtained with `Genoid` please see Table 2 for a description of the listed parameters.

	(3548) Eurybates and Queta	
Observing dataset		
Number of observations	9	
Time span (days)	884	
RMS (mas)	7.89	
Orbital elements EQJ2000		
P (day)	82.5	±0.2
a (km)	2345.5	±43.6
e	0.14	±0.03
i (°)	132.6	±0.6
Ω (°)	193.5	±2.5
ω (°)	15.7	±10.4
t_p (JD)	2458375.07879	±1.88861
Derived parameters		
$M_{\text{Eurybates}}$ ($\times 10^{17}$ kg)	1.502	±0.089
λ_p, β_p (°)	113, –64	±4, 1
α_p, δ_p (°)	104, –43	±3, 1

substantially worse (6.4 mas RMS), but the non-detection is more reasonably placed. This is significantly worse than the precision expected from HST observations, the precision achieved for (22899) Alconrad, based on a very similar dataset, and the precision of many solutions based on ground based observations. However, in light of the smearing issue affecting one in four images, the fit could be acceptable in this instance. This solution provides an eccentricity of ($e \approx 0.18$), and a density of 3.3 ± 0.9 g cm^{-3}, however, the extremely small and poor-quality dataset for Christophedumas means that these results are merely the best approximation possible with the current, very limited dataset, and would benefit significantly from future follow-up observations. All reasonable solutions we have determined require nonzero eccentricity of the satellite.

5.7. (22899) Alconrad

For (22899) Alconrad, we were able to determine an unambiguous orbital solution for the system. From 5 observations, we find an orbital period of 56 days, a semimajor axis of 204 ± 18 km and 1.46 mas RMS residuals. Taking the diameter of 5.2 ± 0.3 km (Sect. 4), we determine a density of 2.9 ± 0.9 g cm^{-3}. This is consistent with the density of Ida and other members of the Koronis family. A detailed description of the orbital solution is reported in Table 7.

6. Discussion

6.1. Proposed formation mechanisms of VWBAs

In the following, we will discuss various mechanisms for VWBA formation that have been proposed by previous authors, including escaping ejecta binaries (EEBs), Binary-YORP (BYORP) spreading, and alternative YORP mechanisms. Following these descriptions, we will discuss the applicability of these models to each of the VWBA systems studied in previous section.

Table 7. Orbital elements of the satellite of Alconrad, expressed in EQJ2000, obtained with `Genoid`; see Table 2 for a description of the listed parameters.

	(22899) Alconrad and Juliekaibarreto	
Observing dataset		
Number of observations	5	
Time span (days)	520	
RMS (mas)	1.46	
Orbital elements EQJ2000		
P (day)	56.29374	±0.14665
a (km)	204.2	±18.0
e	0.132	±0.100
i (°)	149.2	±2.0
Ω (°)	95.4	±3.0
ω (°)	251.5	±15.0
t_p (JD)	2452847.00556	±1.92780
Derived parameters		
M ($\times 10^{14}$ kg)	2.128	±0.561
λ_p, β_p (°)	331, –54	±3, 2
α_p, δ_p (°)	5, –59	±3, 2

6.1.1. Escaping ejecta binary model

The escaping ejecta binary (EEB) model induces binary formation through mutual capture of two (or more) ejecta particles following an impact to a shared parent body (Durda et al. 2004). The chaotic nature of this formation mechanism results in a range of orbital parameters, and predicts a wide range of eccentricity (Durda et al. 2004).

Depending on the specifics of the system, it is possible that eccentricity could be damped over time due to tidal dissipation (Goldreich & Sari 2009). Simulations by Durda et al. (2004) suggest that a large fraction of EEBs could have equal size ratios ($D_s/D_p > 0.5$), however this is most likely an effect of the minimum particle size used in the simulations. The nature of this formation mechanism should favor systems that belong to (large) families, as the same impacts that form these families would produce the ejecta necessary for the formation of these binary systems. It is also possible that the very wide satellites formed as a result of an impact to the primary body of the system (analogous to the SMATs of the Durda et al. (2004) model). This is particularly likely for Eurybates, which is the largest member of the Eurybates family. However, we consider the EEB and SMAT formation scenarios proposed by Durda et al. (2004) to be roughly equivalent, as in the limit of catastrophic disruption where there are several equally large family members instead of a single parent-body remnant there is no meaningful difference between the two. As such, we henceforth refer to these models jointly as the “EEB model”, although we note that this is indeed an oversimplification.

6.1.2. BYORP expansion

The very wide binary asteroid population has also been previous linked to YORP spin-up, a formation mechanism which is expected to have produced the majority of known small ($D < 10$ km) binary asteroid systems, as several members of this population exhibit characteristic YORP formation traits

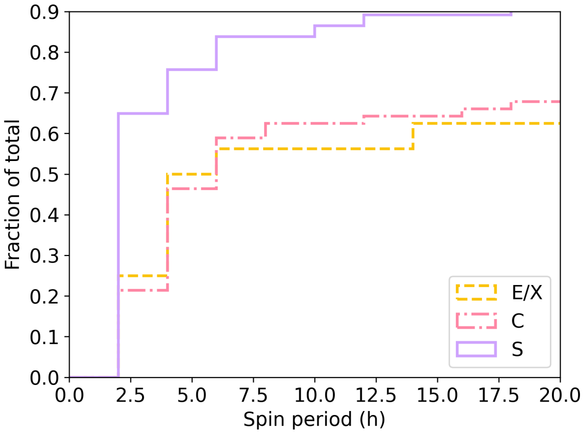

Fig. 6. Cumulative histogram of spin rates for Hungaria family asteroids across different taxonomic types, expressed as a fraction of the total population. Asteroids classified as X-types are assumed to be E-types, and have been grouped together. A total sample of 39 (65, 16) S (C, X/E)-type asteroids with known spin periods were considered. Very slow rotating asteroids (P>100 h) were excluded from the sample. S-type asteroids tend to rotate significantly faster than C or X/E type asteroids. The sample is diameter limited ($2.5\,\mathrm{km} < D < 10\,\mathrm{km}$), with diameters estimated based on the absolute magnitude and average albedo for the taxonomic class (from Mahlke et al. 2022). Analysis without the diameter limitation and sample sizes of 88 (106, 167) S (C, X/E)-type asteroids provide similar results.

($D_s/D_p \approx 0.3$, spin periods ≈2.5 h, Polishook et al. 2011; Pravec & Harris 2007). Binary-YORP (BYORP) effects can influence the orbits of asteroid satellites, causing them to expand or contract, and gain or lose eccentricity (Jacobson et al. 2014).

It is possible that the VWBAs initially form their satellites at close distances ($a \approx 3R_p$), and then BYORP effects expand the orbit to their currently observed very wide positions (Jacobson et al. 2014). Stable BYORP expansion of an asteroid satellite formed through typical YORP spin-up could present a very circular orbit that is co-planar to the spin orientation of the primary, so that the expansion remains stable over time (Ćuk & Burns 2005). BYORP expansion also requires a tidally locked satellite, although systems that were previously expanded by BYORP may have satellites that are no longer tidally locked (Jacobson et al. 2014). There is also a possibility that in some systems BYORP expansion occurs faster than tidal circularization, which could potentially result in a nonzero eccentricity for an expanded system. Similarly, solar tides, which become stronger at greater separations, can act to grow the eccentricity over time, particularly if the heliocentric orbit itself becomes more eccentric. As such, while a perfectly circular orbit for a distant satellite would be a marker of BYORP expansion, the lack thereof does not exclude the possibility of previous BYORP expansion.

Previous studies (Jacobson et al. 2014; Polishook et al. 2011) have argued against the EEB formation scenario in favor of a BYORP scenario for small VWBAs as these systems typically possess rapidly rotating primaries (see Table 1) which are consistent with YORP spin-up. However, rapidly rotating primaries are characteristic of small mafic-silicate rich asteroids in general (see Figure 6), and as such this is insufficient to exclude the EEB scenario. A potential marker of the YORP satellite formation could be an alignment between the satellite's orbital pole and the primary's spin axis, although this may not occur in the case of multiple-satellite interaction. Nevertheless, the observational dataset is currently insufficient to determine the primary spin axis to the necessary precision for most systems, so it is not possible to test. It is also worthy to note that the two scenarios are not mutually exclusive, as a satellite formed through the EEB scenario could later undergo the influences of BYORP, given the appropriate orbital geometry.

6.1.3. Simultaneous YORP formation and scattering

It is also possible that the VWBA population forms through the typical YORP formation pathway with closely orbiting satellites that are then expanded to their current very wide orbits by a mechanism other than BYORP. One dynamical explanation for this could be that in systems with multiple satellites, mutual interactions may occur that scatter one or more of the satellites onto a very wide orbit.

This mechanism is also capable of ejecting one (or more) satellites from the system, forming an asteroid pair. The scattering event could position the satellite at a random inclination or eccentricity, resulting in a wide variety of final orbital geometries. This argument is particularly compelling in systems with multiple known satellites, although it could be consistent with single-satellite systems. For single-satellite systems, it is possible that one satellite is ejected from the system, or that there is an unknown additional satellite orbiting on a moderately-wide orbit that our current detection methods are not robust to. This mechanism is briefly described in Agrusa et al. (2024), as well as Pravec et al. (2019), which notes an overlap between asteroid pair primaries and known (Balam) or suspected very wide satellites. A potential marker of this mechanism would be that the pericenter of the outer satellite be just outside the orbit of the inner satellite, although this is not observed for any of the systems in this study.

6.2. Comparison with observed properties

In general, we find the orbital dynamics of the VWBAs reported in Sect. 5 to be largely incompatible with active BYORP expansion. Of the four small ($D < 10\,\mathrm{km}$) systems for which we were able to develop orbital models, all but Pauling were incompatible with a zero-eccentricity model. Since active BYORP expansion requires the satellite to be on a circular equatorial orbit, these nonzero eccentricities indicate that another mechanism must be fully or partially responsible for the current orbital orientation.

Furthermore, the wide satellites of both Litva and Esclangona are known to have spin periods independent of both the orbital period and primary spin period (Warner 2011a; Warner et al. 2009), prohibiting them from maintaining the tidally locked singly-synchronous geometry required to maintain active BYORP expansion (Ćuk & Burns 2005). For both systems the satellite spin period is very close to twice the primary spin period, varying by a factor of 2.02 and 2.04 respectively. This notable correlation suggests that there may be some kind of ongoing process or formation artifact stabilizing the spins of these outer satellites, or potentially that these spin periods have been misattributed to the outer satellite, and actually belong to some other component of the system. The latter may imply that the fraction of VWBAs is quite large, as this third spin period component was used to predict the discovery of Litva's outer satellite (Pravec et al. 2012b). Furthermore, the successful discovery of a third component based on a misattributed spin period implies that there is a high likelihood of any given binary system containing an additional component (Warner 2011a).

Based on these two pieces of evidence, we determine that the following systems are unlikely to have formed through YORP spin-up followed by BYORP expansion: (1509) Esclangona, (2577) Litva, (22899) Alconrad, and (17246) Christophedumas.

The satellite of (4674) Pauling could plausibly have formed through this scenario, and the orbital solution for (3749) Balam is too poor in quality to make an accurate determination. For these systems, two possibilities remain: the EEB model or an exotic YORP formation mechanism (for example, mutual interactions between satellites, one of which may currently be unbound). For the two large VWBA systems, (379) Huenna and (3548) Eurybates, the EEB model seems most likely. Both systems are associated with large families (Themis and Eurybates), indicating the presence of a major impact in their dynamical history. Both systems exhibit significantly eccentric orbits, aligning with the somewhat random orbital dynamics expected for EEB satellites. Furthermore, YORP spin-up is ineffective for large asteroids, and both systems rotate much slower than necessary for YORP induced satellite formation (7 or 14.1 h for Huenna and 8.7 h for Eurybates, Xu et al. 2023; Warner 2010; Stephens & Warner 2021). Compared to large Main-Belt and Trojan binary systems that are assumed to have formed satellites through large impacts such as (22) Kalliope, (702) Alauda, (283) Emma, (624) Hektor, these slower rotation periods are longer than average, but within the observed range (Carry et al. 2021), further indicating the likelihood of impact formation.

The EEB model is very flexible, and encompasses systems resulting in a wide variety of orbital orientations and component size ratios. Unfortunately, this binary asteroid formation scenario has not been studied rigorously outside of the characterization of the Koronis family by Durda et al. (2004), so it is difficult to assess the exact compatibility of the mechanism with the observed characteristics of VWBA systems. Most known VWBA systems belong to large families, which aligns with the EEB model. It is, however, unclear to what extent the expectation of binary systems to belong to families has introduced an observational bias to the discovery of these systems. For example, Alconrad and Christophedumas were both discovered as part of a targeted study of the Koronis family. The component size ratios (D_s/D_p) of most small VWBA systems is similar to that of most binary systems that have formed through YORP spin-up, but it is unclear to what extent this is an observational bias. Direct imaging of small binary asteroid systems already poses a significant challenge, and it is possible that a small system with the extreme component size ratios observed in large ($D > 50$ km) VWBA systems is beyond our current detection limits.

There remain several points of evidence linking VWBA systems to some sort of YORP formation: many systems have very fast primary spin periods, and the D_s/D_p ratio is in line with that of the population of closely-orbiting binaries of YORP formation, although this may be influenced by observational biases. These similarities could imply that a more exotic YORP mechanism involving multiple satellites and/or pair formation is the source of VWBA systems. However, YORP can spin up an object without forming a satellite, (Zhang et al. 2022) so a certain level of skepticism should be applied to this thinking. This is taxonomically linked, as dark taxonomic types are more likely to deform under slower rotations. YORP spin-up seems to be very effective on small, S-type asteroids, causing S-type objects to reach much faster rotation rates than C- or E-type objects in the same dynamical populations (Figure 6).

This likely contributes to the general overabundance of silicate compositions amongst YORP-induced binary systems (Minker & Carry 2023), but the correlation in spin rates amongst taxonomic types can also be seen in the general asteroid population. Due to the limiting magnitude of adaptive-optics instruments, small asteroids of dark taxonomic types are necessarily impossible to observe under normal circumstances. As such, no small VWBA systems with dark taxonomic types have been identified, although dark taxonomic types dominate the large VWBA systems. It is impossible to know if the absence of VWBA systems amongst dark taxonomic types is a true quality of the population or merely an artifact of observational bias.

We find Litva to be notably less dense than Pauling and other small S-type asteroids (Chabot et al. 2024; Carry et al. 2012). The extremely high albedo of the system (0.56, Alí-Lagoa & Delbo’ 2017) suggests that it is unlikely that this low density results from an overestimate of the diameter of the system. It is possible that this value for Litva’s albedo is overestimated (see alternative H_V estimate in Pravec et al. 2012a), but correcting for this Litva is still brighter than average for an S-type asteroid ($p_V = 0.41 \pm 0.08$). Spectral analysis (Mahlke et al. 2022) confirms that Litva is an S-type asteroid, rather than a misclassified E-type. Extremely high albedos can be observed in other Hungaria-family asteroids with clear silicate features in their spectra, such as (1727) Mette.

Among small VWBA systems, we notice a correlation between the number of satellites possessed by a system and the eccentricity of the system’s wide satellite. The only object in this study was an eccentricity compatible with a perfectly circular orbit, (4674) Pauling, is also the only system with enough light curve observations to indicate the absence of an inner satellite (Warner et al. 2006; Warner 2011b). (2577) Litva has an inner satellite and a high eccentricity, as does (3749) Balam (although in the latter case this eccentricity is poorly defined). Balam is also a member of a pair, which can be considered as an escaped satellite with eccentricity >1. This indicates the possibility that the inner satellite may be influencing the eccentricity of the outer satellite, and could therefore indicate an undetected inner satellite for other eccentric VWBA systems, such as (379) Huenna. A summary of satellite eccentricities for the VWBAs can be found in Figure 7. Although we note a trend between multiplicity and high eccentricities, the relationship is not necessarily causal, but is worth exploring in future work.

This spin period ratio also denotes a contrast to the wide binary systems discussed in various works by Warner et al. (Warner & Stephens 2020, 2019; Warner 2016, to name a few), which propose a sample of objects with long (10s-100s of hours) primary spin periods and short secondary spin periods, marking a binary system with a primary that has been spun-down by YORP. This is inconsistent with the sample we present, all of which have fast primary spin periods, with the exception of Christophedumas, for which the spin period is uncertain. However, some of the proposed wide binary systems are consistent with the remote sensing properties of (152830) Dinkinesh, for which the dominant 53 h period presented by Mottola et al. (2023a) is actually associated to the bi-lobated satellite and not the primary, as initially assumed. It may be worthwhile to consider the possibility that these objects could have extremely elongated, tidally locked satellites (corresponding to the higher-amplitude, slower period) and nearly spherical primaries (corresponding to the lower-amplitude, faster period) causing them to present this unusual profile.

6.3. Limitations

With the exception of (379) Huenna, the orbital datasets in this study are sparse, containing few observations with large gaps between them. This allows for potential aliasing in orbit determination, and limits the precision of the presented solutions.

We encourage future observations of these systems to help resolve these degeneracies and improve the quality of

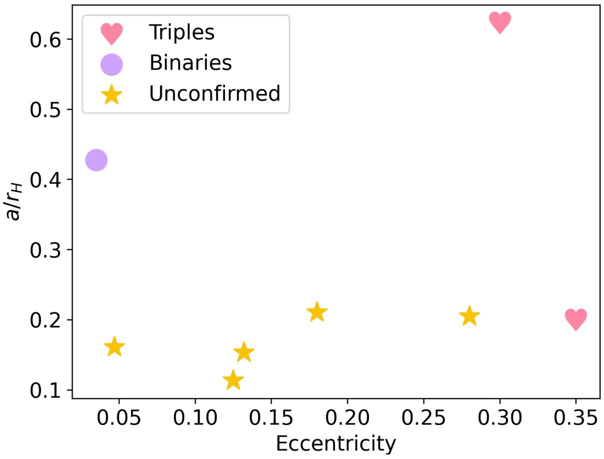

Fig. 7. Normalized semimajor axis vs. eccentricities of VWBA systems. Systems with confirmed inner satellites are very eccentric, whereas those with only one satellite are nearly circular. Objects marked 'unconfirmed' are those for which current observations are insufficient to detect a satellite of similar size to the known satellite orbiting close to the system's primary. Both solutions for Christophedumas are represented, and the eccentricity and semimajor axis of Balam is approximated based off preliminary orbital solutions. Satellite eccentricity appears to be independent of semimajor axis.

these orbits, particularly in the case of Balam, which is a rare triple+pair system. Although these objects have not been observed in many years, these gaps in the observational history should be relatively easy to reconcile due to the extremely long orbital periods of the systems.

7. Conclusions

We have presented observations and orbital analysis of seven multiple systems of asteroids belonging to the class of very wide binary asteroids, of which we were able to develop an orbital solution for five systems. We have gathered and reported high-angular-resolution images of each system, mid-infrared photometry for (17246) Christophedumas and (22899) Alconrad, and optical light curves for (2577) Litva. For all systems except Christophedumas, Esclangona, and Balam, we constrain the orbit of the satellite with high accuracy. We report orbital solutions for the first time for Pauling, Alconrad and Christophedumas, and improve or confirm the dynamics of Litva, Huenna, and Eurybates. We also reject the previously published solution of Balam's outer satellite, but are unable to offer a new, more accurate solution with the available archival data. The analysis of the mid-infrared photometry provides the diameter and albedo of Alconrad and Christophedumas. We report the density of Alconrad, Litva, and Pauling for the first time. Based on the properties of the systems, we determine that only (4674) Pauling could be compatible with the BYORP expansion model of VWBA formation. Other systems in this sample could be compatible with a more exotic YORP formation mechanism or an EEB model. An apparent correlation between systems with at least two satellites and highly eccentric orbits implies that an inner satellite can play a role in shepherding the eccentricity of the very wide outer satellite, a mechanism that could also apply to the large-diameter very wide systems (379) Huenna and (3548) Eurybates.

Acknowledgements. We wish to thank Harrison Agrusa for his very helpful commentary. The work by P.S. and P.P. was supported by the Grant Agency of the Czech Republic, Grant 23-04946S. M.H. thanks the Slovak Grant Agency for Science VEGA (grant No. 2/0059/22) and M. Pikler for many observations. J.V. and Š.G. thank the Slovak Grant Agency for Science VEGA (grant 1/0530/22). TRAPPIST is funded by the Belgian Fund for Scientific Research (FNRS) under the grant PDR T.0120.21. E.J. is a FNRS Senior Research Associate. Observational work at the Sopot Observatory in Serbia by V. Benishek was generously supported by Shoemaker NEO Grants in 2018 and 2022 from the Planetary Society. Work at Sugarloaf Mountain Observatory was also made possible by Gene Shoemaker NEO grants from the Planetary Society. This research has made use of the Keck Observatory Archive (KOA), which is operated by the W.M. Keck Observatory and the NASA Exoplanet Science Institute (NExScI), under contract with the National Aeronautics and Space Administration. Some of the data presented herein were obtained at Keck Observatory, which is a private 501(c)3 non-profit organization operated as a scientific partnership among the California Institute of Technology, the University of California, and the National Aeronautics and Space Administration. The Observatory was made possible by the generous financial support of the W.M. Keck Foundation. The authors wish to recognize and acknowledge the very significant cultural role and reverence that the summit of Maunakea has always had within the Native Hawaiian community. We are most fortunate to have the opportunity to conduct observations from this mountain. This publication makes use of data products from the Wide-field Infrared Survey Explorer, which is a joint project of the University of California, Los Angeles, and the Jet Propulsion Laboratory/California Institute of Technology, funded by the National Aeronautics and Space Administration. This work is based in part on observations made with the Spitzer Space Telescope, which was operated by the Jet Propulsion Laboratory, California Institute of Technology under a contract with NASA. The LBT is an international collaboration among institutions in the United States, Italy and Germany. LBT Corporation Members are: The University of Arizona on behalf of the Arizona Board of Regents; Istituto Nazionale di Astrofisica, Italy; LBT Beteiligungsgesellschaft, Germany, representing the Max-Planck Society, The Leibniz Institute for Astrophysics Potsdam, and Heidelberg University; The Ohio State University, representing OSU, University of Notre Dame, University of Minnesota and University of Virginia. This publication has made use of the Canadian Astronomy Data Centre moving object search tool (Gwyn et al. 2012). This research used the `Miriade` (Berthier et al. 2009), `SsODNet` (Berthier et al. 2023), and `TOPCAT` (Taylor 2005) Virtual Observatory tools. Some of the work presented here is based on observations collected at the European Organisation for Astronomical Research in the Southern Hemisphere under ESO program 074.C-0052 and 089.C-0944 (PI Marchis), 71.C-0669, 072.C-0753 (PI:Merline). This research is based on observations made with the NASA/ESA Hubble Space Telescope obtained from the Space Telescope Science Institute, which is operated by the Association of Universities for Research in Astronomy, Inc., under NASA contract NAS 5–26555. These observations are associated with program(s) 10165 and 9747.

References

Agrusa, H. F., Zhang, Y., Richardson, D. C., et al. 2024, Pla. Sci. Journal, 5, 54
Alí-Lagoa, V., & Delbo', M. 2017, A&A, 603, A55
Benishek, V. 2019, Minor Planet Bull., 46, 87
Berthier, J. 1998, Notes scientifique et techniques du Bureau des longitudes, S061
Berthier, J., Vachier, F., Thuillot, W., et al. 2006, ASP Conf. Ser., 351, 367
Berthier, J., Hestroffer, D., Carry, B., et al. 2009, Eur. Planet. Sci. Congress, 2009, 676
Berthier, J., Vachier, F., Marchis, F., Ďurech, J., & Carry, B. 2014, Icarus, 239, 118
Berthier, J., Carry, B., Vachier, F., Eggl, S., & Santerne, A. 2016, MNRAS, 458, 3394
Berthier, J., Carry, B., Mahlke, M., & Normand, J. 2023, A&A, 671, A151
Brown, M. E., Levison, H. F., Noll, K. S., et al. 2021, Pla. Sci. Journal, 2, 170
Brož, M., Marchis, F., Jorda, L., et al. 2021, A&A, 653, A56
Brozović, M., Benner, L. A. M., Taylor, P. A., et al. 2011, Icarus, 216, 241
Carry, B. 2012, Planet. Space Sci., 73, 98
Carry, B., & Berthier, J. 2018, Planet. Space Sci., 164, 79
Carry, B., Dumas, C., Fulchignoni, M., et al. 2008, A&A, 478, 235
Carry, B., Kaasalainen, M., Merline, W. J., et al. 2012, Planet. Space Sci., 66, 200
Carry, B., Vachier, F., Berthier, J., et al. 2019, A&A, 623, A132
Carry, B., Vernazza, P., Vachier, F., et al. 2021, A&A, 650, A129
Chabot, N. L., Rivkin, A. S., Cheng, A. F., et al. 2024, Pla. Sci. Journal, 5, 49
Chapman, C. R., Veverka, J., Thomas, P. C., et al. 1995, Nature, 374, 783
Ćuk, M., & Burns, J. A. 2005, Icarus, 176, 418
Dolphin, A. E. 2000, PASP, 112, 1383
Dolphin, A. 2016, Astrophysics Source Code Library [record `ascl:1608.013`]
Durda, D. D., Bottke, W. F., Enke, B. L., et al. 2004, Icarus, 167, 382
Fang, J., & Margot, J.-L. 2012, AJ, 143, 25
Fazio, G. G., Hora, J. L., Allen, L. E., et al. 2004, ApJS, 154, 10
Goldreich, P., & Sari, R. 2009, ApJ, 691, 54
Gwyn, S. D. J., Hill, N., & Kavelaars, J. J. 2012, PASP, 124, 579
Harris, A. W. 1998, Icarus, 131, 291
Herrera, C., Carry, B., Lagain, A., & Vavilov, D. E. 2024, A&A, 688, A176

Jacobson, S. A., & Scheeres, D. J. 2011, Icarus, 214, 161
Jacobson, S. A., Scheeres, D. J., & McMahon, J. 2014, ApJ, 780, 60
Jehin, E., Gillon, M., Queloz, D., et al. 2011, The Messenger, 145, 2
Kaasalainen, M., & Torppa, J. 2001, Icarus, 153, 24
Kaasalainen, M., Mottola, S., & Fulchignoni, M. 2002, Asteroids III, 139
Lagerros, J. S. V. 1996a, A&A, 310, 1011
Lagerros, J. S. V. 1996b, A&A, 315, 625
Lagerros, J. S. V. 1997, A&A, 325, 1226
Lagerros, J. S. V. 1998, A&A, 332, 1123
Landolt, A. U. 1992, AJ, 104, 340
Lenzen, R., Hartung, M., Brandner, W., et al. 2003, SPIE, 4841, 944
Levison, H. F., Olkin, C. B., Noll, K. S., et al. 2021, Pla. Sci. Journal, 2, 171
Levison, H. F., Marchi, S., Noll, K. S., et al. 2024, Nature, 629, 1015
Liberato, L., Tanga, P., Mary, D., et al. 2024, A&A, 688, A50
Mahlke, M., Carry, B., & Denneau, L. 2021, Icarus, 354, 114094
Mahlke, M., Carry, B., & Mattei, P. A. 2022, A&A, 665, A26
Manek, J., Dramonis, S., & Weber, C. 2023, Central Bureau Electron. Telegrams, 5318, 1
Marchis, F., Descamps, P., Berthier, J., et al. 2008, Icarus, 195, 295
Margot, J.-L., Pravec, P., Taylor, P., Carry, B., & Jacobson, S. 2015, Asteroid Systems: Binaries, Triples, and Pairs, eds. P. Michel, F. DeMeo, & W. F. Bottke (University of Arizona Press), 355
Masiero, J. R., Mainzer, A. K., Grav, T., et al. 2011, ApJ, 741, 68
Masiero, J. R., Mainzer, A. K., & Wright, E. L. 2018, AJ, 156, 62
Merline, W. J., Close, L. M., Siegler, N., et al. 2002, IAU Circ., 7827, 2
Merline, W. J., Close, L. M., Tamblyn, P. M., et al. 2003a, IAU Circ., 8075, 2
Merline, W. J., Tamblyn, P. M., Chapman, C. R., et al. 2003b, IAU Circ., 8232, 2
Merline, W. J., Tamblyn, P. M., Dumas, C., et al. 2004, IAU Circ., 8297, 1
Merline, W. J., Tamblyn, P. M., Warner, B. D., et al. 2013a, IAU Circ., 9267, 1
Merline, W. J., Tamblyn, P. M., Warner, B. D., et al. 2013b, Central Bureau Electron. Telegrams, 3765, 1
Minker, K., & Carry, B. 2023, A&A, 672, A48
Montaigut, R., Christmann, B., Conjat, M., et al. 2019, in SF2A-2019: Proceedings of the Annual meeting of the French Society of Astronomy and Astrophysics, eds. P. Di Matteo, O. Creevey, A. Crida, et al.
Mottola, S., Denk, T., Marchi, S., et al. 2023a, MNRAS, 524, L1
Mottola, S., Hellmich, S., Buie, M. W., et al. 2023b, Pla. Sci. Journal, 4, 18
Müller, T. G., & Lagerros, J. S. V. 1998, A&A, 338, 340
Müller, T. G., Micheli, M., Santana-Ros, T., et al. 2023, A&A, 670, A53
Myhrvold, N., Pinchuk, P., & Margot, J.-L. 2022, Pla. Sci. Journal, 3, 30
Noll, K., Brown, M., Weaver, H., et al. 2020, Minor Planet Electronic Circulars, 2020-A113
Noll, K. S., Brown, M. E., Buie, M. W., et al. 2023, Space Sci. Rev., 219, 59
Ostro, S. J., Margot, J.-L., Benner, L. A. M., et al. 2006, Science, 314, 1276
Ou, J., Baranec, C., & Bus, S. J. 2022, Pla. Sci. Journal, 3, 169
Pajuelo, M., Carry, B., Vachier, F., et al. 2018, Icarus, 309, 134
Parker, A. H., Kavelaars, J. J., Petit, J.-M., et al. 2011, ApJ, 743, 1
Petit, J. M., Durda, D. D., Greenberg, R., Hurford, T. A., & Geissler, P. E. 1997, Icarus, 130, 177
Polishook, D., & Aharonson, O. 2020, Icarus, 336, 113415
Polishook, D., Brosch, N., & Prialnik, D. 2011, Icarus, 212, 167
Pravec, P., & Harris, A. W. 2007, Icarus, 190, 250
Pravec, P., Vokrouhlický, D., Polishook, D., et al. 2010, Nature, 466, 1085
Pravec, P., Harris, A. W., Kušnirák, P., Galád, A., & Hornoch, K. 2012a, Icarus, 221, 365
Pravec, P., Scheirich, P., Vokrouhlický, D., et al. 2012b, Icarus, 218, 125
Pravec, P., Scheirich, P., Ďurech, J., et al. 2014, Icarus, 233, 48
Pravec, P., Scheirich, P., Kušnirák, P., et al. 2016, Icarus, 267, 267
Pravec, P., Fatka, P., Vokrouhlický, D., et al. 2019, Icarus, 333, 429
Pravec, P., Thomas, C. A., Rivkin, A. S., et al. 2022, Pla. Sci. Journal, 3, 175
Rousset, G., Lacombe, F., Puget, P., et al. 2003, SPIE, 4839, 140
Ryon, J. E., & Stark, D. V. 2023, in ACS Instrument Handbook for Cycle 32 v. 23.0, 23
Scheirich, P., & Pravec, P. 2009, Icarus, 200, 531
Scheirich, P., & Pravec, P. 2022, Pla. Sci. Journal, 3, 163
Scheirich, P., Pravec, P., Jacobson, S. A., et al. 2015, Icarus, 245, 56
Scheirich, P., Pravec, P., Kušnirák, P., et al. 2021, Icarus, 360, 114321
Sergeyev, A. V., & Carry, B. 2021, A&A, 652, A59
Shevchenko, V. G., Belskaya, I. N., Slyusarev, I. G., et al. 2022, A&A, 666, A190
Stephens, R. D., & Warner, B. D. 2021, Minor Planet Bull., 48, 13
Szakáts, R., Müller, T., Alí-Lagoa, V., et al. 2020, A&A, 635, A54
Tamblyn, P. M., Merline, W. J., Chapman, C. R., et al. 2004, IAU Circ., 8293, 3
Taylor, M. B. 2005, ASP Conf. Ser., 347, 29
Vachier, F., Berthier, J., & Marchis, F. 2012, A&A, 543, A68
Vachier, F., Carry, B., & Berthier, J. 2022, Icarus, 382, 115013
van Dam, M. A., Le Mignant, D., & Macintosh, B. 2004, Appl. Opt., 43, 5458
Vavilov, D. E., Carry, B., Lagain, A., et al. 2022, Icarus, 383, 115045
Vernazza, P., Ferrais, M., Jorda, L., et al. 2021, A&A, 654, A56
Vokrouhlický, D., Bottke, W. F., Chesley, S. R., Scheeres, D. J., & Statler, T. S. 2015, in Asteroids IV, 509
Walsh, K. J., Richardson, D. C., & Michel, P. 2008, Nature, 454, 188
Warner, B. D. 2010, Minor Planet Bull., 37, 112
Warner, B. D. 2011a, Minor Planet Bull., 38, 33
Warner, B. D. 2011b, Minor Planet Bull., 38, 25
Warner, B. D. 2016, Minor Planet Bull., 43, 306
Warner, B. D., & Stephens, R. D. 2019, Minor Planet Bull., 46, 153
Warner, B. D., & Stephens, R. D. 2020, Minor Planet Bull., 47, 37
Warner, B. D., Pravec, P., Kusnirák, P., et al. 2006, Minor Planet Bull., 33, 34
Warner, B. D., Pravec, P., Kusnirak, P., et al. 2009, Central Bureau Electron. Telegrams, 2020, 1
Waszczak, A., Chang, C.-K., Ofek, E. O., et al. 2015, AJ, 150, 75
Wright, E. L., Eisenhardt, P. R. M., Mainzer, A. K., et al. 2010, AJ, 140, 1868
Xu, X., Wang, X., Muinonen, K., et al. 2023, MNRAS, 521, 3925
Yang, B., Hanuš, J., Carry, B., et al. 2020, A&A, 641, A80
Zhang, Y., Michel, P., Barnouin, O. S., et al. 2022, Nat. Commun., 13, 4589

---

[1] Université Côte d'Azur, Observatoire de la Côte d'Azur, CNRS, Laboratoire Lagrange, Bd de l'Observatoire, CS 34229, 06304 Nice cedex 4, France
[2] IMCCE, Observatoire de Paris, PSL Research University, CNRS, Sorbonne Universités, UPMC Univ Paris 06, Univ. Lille, 75014 Paris, France
[3] Astronomical Institute AS CR, Fričova 298, Ondřejov, Czech Republic
[4] Max-Planck-Institut für extraterrestrische Physik, Giessenbachstraße, Postfach 1312, 85741 Garching, Germany
[5] Konkoly Observatory, HUN-REN Research Centre for Astronomy and Earth Sciences, Konkoly-Thege Miklós út 15–17, 1121 Budapest, Hungary
[6] INAF – Osservatorio Astronomico di Padova, Vicolo dell'Osservatorio 5, 35122 Padova, Italy
[7] Large Binocular Telescope Observatory, University of Arizona, Tucson, AZ 85721, USA
[8] Department of Earth & Environmental Sciences, Michigan State University, East Lansing, MI 48824, USA
[9] European Southern Observatory (ESO), Alonso de Cordova 3107, 1900 Casilla Vitacura, Santiago, Chile
[10] Southwest Research Institute, 1301 Walnut St. #400, Boulder, CO 80302, USA
[11] Division of Geological and Planetary Sciences, California Institute of Technology, Pasadena, CA 91125, USA
[12] Sugarloaf Mountain Observatory, South Deerfield, MA, USA
[13] Observatoire OPERA, 33820 Saint-Palais, France
[14] Astronomical Institute of the Slovak Academy of Sciences, SK-05960 Tatranská Lomnica, The Slovak Republic
[15] Belgrade Astronomical Observatory, Volgina 7, 11060 Belgrade 38, Serbia
[16] Sonoita Research Observatory, 77 Paint Trail, Sonoita, AZ 85637, USA
[17] Space sciences, Technologies & Astrophysics Research (STAR) Institute, University of Liege, Liege, Belgium
[18] Modra Observatory, Department of Astronomy, Physics of the Earth, and Meteorology, FMPI UK, Mlynská dolina, Bratislava 84248, Slovakia
[19] Department of Astronomy, Physics of the Earth, and Meteorology, FMPI, Comenius University, Mlynská Dolina F1, Bratislava 84248, Slovakia
[20] Institute of Astronomy of V.N. Karazin Kharkiv National University, Kharkiv 61022, Sumska Str. 35, Ukraine
[21] Observatoire La Souchère, 69510 Soucieu-en-Jarrest, France
[22] Via Capote Observatory, Thousand Oaks, CA 91320, USA
[23] Royal Observatory Edinburgh, Blackford Hill, Edinburgh, EH9 3HJ, UK
[24] Currently at NOIRLab/Gemini Observatory, 950 N Cherry Ave, Tucson, AZ, 85719, USA
[25] Lowell Observatory, 1400 W. Mars Hill Rd., Flagstaff, AZ 86001, USA
[26] Steward Observatory, N420, Department of Astronomy, University of Arizona, 933 N. Cherry Ave. Tucson, AZ 85721, USA

Appendix A: Astrometry and photometry of the VWBA satellites

We list in the following tables the relative astrometry and photometry of the satellites of (379) Huenna (Table A.1), (2577) Litva (Table A.2), (3548) Eurybates(Table A.3), (3749) Balam (Table A.4), (4674) Pauling (Table A.5), (17246) Christophedumas (Table A.6), and (22899) Alconrad (Table A.7).

Table A.1: Astrometry of (379) Huenna's satellite S/2003 (379) 1.

Date	UTC	Tel.	Cam.	Filter	X_o (mas)	Y_o (mas)	X_{o-c} (mas)	Y_{o-c} (mas)	σ (mas)	ΔM (mag)	δM (mag)
2003-08-14	13:04:25.90	Keck II	NIRC2	H	501.6	737.0	0.3	4.0	10.0	8.1	0.6
2003-08-14	14:07:52.88	Keck II	NIRC2	H	506.3	737.3	-3.3	-0.3	10.0	7.8	0.3
2003-08-15	13:34:46.63	Keck II	NIRC2	Kp	693.1	838.7	0.4	0.6	10.0	7.0	0.1
2003-08-15	13:38:59.65	Keck II	NIRC2	Kp	696.3	841.7	3.1	3.3	10.0	7.1	0.1
2003-08-17	14:53:55.04	Keck II	NIRC2	Kp	1070.0	1028.6	1.2	-7.3	10.0	7.1	0.1
2003-08-18	14:19:56.05	Keck II	NIRC2	Kp	1243.2	1116.1	1.6	-6.7	10.0	6.9	0.0
2004-12-08	07:00:25.58	ESO-VLT	NACO	Ks	1771.2	114.2	-8.2	-10.9	13.3	6.3	0.6
2004-12-08	07:08:31.34	ESO-VLT	NACO	Ks	1783.4	130.1	4.1	4.8	13.3	7.4	0.8
2004-12-09	06:29:18.80	ESO-VLT	NACO	Ks	1759.3	147.5	13.6	-2.7	13.3	6.5	0.4
2004-12-09	06:41:52.74	ESO-VLT	NACO	Ks	1743.5	146.8	-1.8	-3.7	13.3	6.9	0.0
2004-12-10	06:45:20.88	ESO-VLT	NACO	Ks	1702.2	176.5	0.8	1.1	13.3	6.4	0.6
2004-12-10	06:51:28.80	ESO-VLT	NACO	Ks	1697.7	174.4	-3.5	-1.1	13.3	6.7	0.0
2004-12-14	05:28:42.92	ESO-VLT	NACO	Ks	1447.4	264.8	-2.2	1.3	13.3	6.7	0.1
2004-12-14	07:08:56.99	ESO-VLT	NACO	Ks	1448.6	266.8	4.4	1.9	13.3	6.7	0.1
2004-12-15	05:20:24.80	ESO-VLT	NACO	Ks	1370.4	285.3	1.0	2.6	13.3	6.9	0.1
2004-12-28	05:36:53.11	ESO-VLT	NACO	Ks	-21.5	396.2	2.1	0.3	13.3	7.1	0.3
2004-12-28	07:41:12.80	ESO-VLT	NACO	Ks	-41.1	397.2	-7.3	1.5	13.3	7.0	0.4
2004-12-29	05:13:34.33	ESO-VLT	NACO	Ks	-141.3	391.0	-1.3	-2.3	13.3	6.3	0.0
2005-01-18	03:58:33.89	ESO-VLT	NACO	Ks	-1924.7	65.5	3.9	5.1	13.3	7.0	0.1
2005-01-18	06:17:33.16	ESO-VLT	NACO	Ks	-1931.5	56.4	0.3	-1.6	13.3	6.7	0.1
2005-01-21	02:25:25.00	ESO-VLT	NACO	Ks	-1991.4	-15.5	-4.6	-2.4	13.3	6.8	0.5
2005-01-25	04:51:31.42	ESO-VLT	NACO	Ks	-1916.0	-110.6	-2.3	-1.1	13.3	7.4	0.0
2005-01-26	02:47:39.26	ESO-VLT	NACO	Ks	-1868.8	-127.0	0.7	1.8	13.3	6.9	0.0
2005-01-26	05:10:41.18	ESO-VLT	NACO	Ks	-1860.3	-127.9	3.7	3.0	13.3	7.4	0.3
2005-01-27	03:10:50.52	ESO-VLT	NACO	Ks	-1799.4	-146.9	7.9	2.0	13.3	7.1	0.2
2005-01-28	03:04:35.77	ESO-VLT	NACO	Ks	-1734.0	-166.3	-1.2	0.5	13.3	6.7	0.3
2005-01-28	03:13:54.04	ESO-VLT	NACO	H	-1735.4	-159.6	-3.1	7.4	13.3	7.4	0.1
2005-02-02	03:09:16.21	ESO-VLT	NACO	Ks	-1147.8	-222.3	1.8	0.8	13.3	7.1	0.0
2005-02-02	05:09:29.47	ESO-VLT	NACO	Ks	-1134.4	-225.9	2.6	-2.4	13.3	7.0	0.1
2005-02-04	02:41:04.73	ESO-VLT	NACO	Ks	-823.5	-223.4	6.1	1.9	13.3	7.0	0.2
2005-02-04	04:05:56.80	ESO-VLT	NACO	Ks	-819.9	-224.2	-0.4	1.0	13.3	6.8	0.1
2005-02-16	01:21:08.59	ESO-VLT	NACO	Ks	1221.4	-4.4	-3.7	-0.4	13.3	6.7	0.3
2009-11-28	12:13:35.10	Keck II	NIRC2	Kp	-1672.8	-616.3	-4.8	6.6	10.0	7.2	0.1
2009-11-28	12:51:36.23	Keck II	NIRC2	Kp	-1673.5	-615.8	-8.5	5.7	10.0	7.0	0.0
2012-02-03	13:18:43.99	Keck II	NIRC2	Kp	740.2	-551.1	-6.5	-2.7	10.0	6.9	0.4
2012-02-03	13:33:28.73	Keck II	NIRC2	Kp	739.6	-552.9	-7.9	-4.4	10.0	7.0	0.1
2012-03-04	10:33:13.88	Keck II	NIRC2	Kp	-1225.8	894.4	4.1	17.5	10.0	7.4	0.3
2012-03-04	10:46:09.13	Keck II	NIRC2	Kp	-1227.3	887.6	3.4	10.4	10.0	7.1	0.6
2012-03-29	07:16:52.32	Keck II	NIRC2	Kp	-1881.0	656.1	-0.5	2.7	10.0	6.9	0.0
2012-06-02	00:51:58.54	ESO-VLT	NACO	Ks	-1568.6	825.2	-13.4	-18.9	13.3	7.0	0.3
2014-12-07	05:38:57.20	Keck II	NIRC2	Ks	-554.1	-585.5	-3.5	-1.4	10.0	6.7	0.0
2021-11-18	15:05:27.27	Keck II	NIRC2	H	-1859.6	175.3	4.4	-12.7	10.0	8.2	0.1

Date, mid-observing time (UTC), telescope, camera, filter, astrometry (X is aligned with Right Ascension, and Y with Declination, and o and c indices stand for observed and computed positions), astrometric uncertainty in X and Y (σ) which are based on the pixel size and performance of the instrument, and photometry (magnitude difference ΔM with uncertainty δM).

Table A.2: Astrometry of (2577) Litva's satellite S/2012 (2577) 1, see Table A.1 for a description of the columns.

Date	UTC	Tel.	Cam.	Filter	X_o (mas)	Y_o (mas)	X_{o-c} (mas)	Y_{o-c} (mas)	σ (mas)	ΔM (mag)	δM (mag)
2004-03-04	09:51:35.99	ESO-VLT	NACO	Ks	174.6	-0.3	1.3	2.0	27.1	6.4	0.0
2012-06-27	07:41:16.71	Keck II	NIRC2	Kp	202.2	-19.1	-0.8	2.7	10.0	3.0	0.1
2012-06-27	07:52:35.87	Keck II	NIRC2	H	200.4	-23.1	-2.6	-1.2	10.0	3.1	0.2
2012-06-27	08:01:13.24	Keck II	NIRC2	J	197.3	-18.9	-5.6	3.0	10.0	3.5	0.4
2012-06-27	09:23:57.44	Keck II	NIRC2	Kp	200.1	-23.8	-2.4	-1.7	10.0	4.1	0.1
2012-08-11	06:36:45.38	Keck II	NIRC2	Kp	-201.1	-49.3	8.8	-0.8	10.0	3.8	0.1
2012-08-11	06:44:44.32	Keck II	NIRC2	Kp	-201.9	-46.1	8.0	2.4	10.0	3.6	0.1
2012-08-16	06:03:29.88	Keck II	NIRC2	Kp	-234.5	-44.9	-2.7	-2.3	10.0	3.1	0.0
2013-08-26	13:59:01.66	Keck II	NIRC2	Kp	-243.2	30.8	-1.2	1.2	10.0	3.2	0.1
2013-08-26	14:05:55.32	Keck II	NIRC2	H	-238.3	26.8	3.7	-2.8	10.0	3.1	0.3
2013-08-26	14:11:23.66	Keck II	NIRC2	Kp	-244.3	32.1	-2.3	2.5	10.0	3.5	0.1
2013-08-26	15:16:01.64	Keck II	NIRC2	Kp	-242.8	32.4	-1.0	2.8	10.0	3.3	0.1
2013-08-27	12:10:53.70	Keck II	NIRC2	Kp	-238.0	24.3	0.2	-6.0	10.0	2.8	0.1
2013-08-27	12:16:00.94	Keck II	NIRC2	H	-237.2	33.1	1.0	2.8	10.0	3.4	0.1
2013-08-27	12:19:18.75	Keck II	NIRC2	H	-240.7	30.6	-2.5	0.3	10.0	3.0	0.1
2013-08-27	12:21:13.16	Keck II	NIRC2	H	-241.2	30.8	-3.0	0.5	10.0	3.0	0.1
2013-08-27	12:24:12.19	Keck II	NIRC2	Kp	-238.7	30.7	-0.5	0.4	10.0	3.0	0.1
2013-08-27	15:03:46.99	Keck II	NIRC2	Kp	-239.0	31.5	-1.3	1.1	10.0	2.8	0.0
2013-08-27	15:07:54.30	Keck II	NIRC2	H	-236.4	32.0	1.3	1.6	10.0	2.9	0.0
2013-10-12	08:56:11.16	LBTO	PISCES	H	439.1	-102.5	0.8	-7.3	19.2	4.4	0.3
2013-10-25	08:47:47.60	Keck II	NIRC2	H	594.8	-103.7	1.1	2.0	10.0	3.3	0.0
2013-10-25	08:51:27.44	Keck II	NIRC2	H	597.6	-103.9	3.8	1.8	10.0	3.3	0.0

Table A.3: Astrometry of Eurybates' satellite Queta with HST/WFC3, see Table A.1 for a description of the columns.

Date	UTC	Filter	X_o (mas)	Y_o (mas)	X_{o-c} (mas)	Y_{o-c} (mas)	σ (mas)	ΔM (mag)	δM (mag)
2018-09-12	09:45:12.96	F555W	-484.9	-103.0 *	15.2	-6.2	11.0	1.0	1.0
2018-09-14	09:26:21.12	F555W	-430.1	-67.0 *	4.3	-21.8	16.0	1.0	1.0
2020-01-03	07:33:27.36	F350LP	-396.5	-408.0 *	1.0	-5.2	5.0	1.0	1.0
2020-07-19	20:40:16.32	F350LP	430.5	460.0	6.6	-0.2	3.0	1.0	1.0
2020-10-12	19:08:15.36	F606W/F814W	504.1	546.0	-3.0	-7.7	5.0	1.0	1.0
2020-10-16	15:17:08.16	F606W/F814W	438.2	487.0	-5.3	-4.4	15.0	1.0	1.0
2020-11-24 *	08:40:07.68	F606W/F814W	-551.4	-605.0	1.3	-5.9	5.0	1.0	1.0
2021-02-10	06:33:59.04	F350LP	-440.3	-462.0	-4.6	4.1	5.0	1.0	1.0
2021-02-12	15:45:12.96	F350LP	-434.1	-476.0	9.3	-3.3	4.0	1.0	1.0

Reproduced from Brown et al. (2021) with minor corrections, astrometry with corrected sign errors is marked with a '*', as are corrected dates. Positions displayed in Figure 1 and JD in Table 2 of Brown et al. (2021) are all correct.

Table A.4: Astrometry of (3749) Balam's satellite S/2002 (3749) 1, see Table A.1 for a description of the columns.

Date	UTC	Tel.	Cam.	Filter	X_o (mas)	Y_o (mas)	X_{o-c} (mas)	Y_{o-c} (mas)	σ (mas)	ΔM (mag)	δM (mag)
2004-12-03	04:00:53.62	ESO/VLT	NACO	Ks	-303.5	83.9	1.6	-2.7	27.1	3.4	0.0
2004-12-07	03:00:08.90	ESO/VLT	NACO	Ks	-339.5	83.0	7.0	2.4	27.1	6.0	0.0
2004-12-09	02:44:09.63	ESO/VLT	NACO	Ks	-377.1	76.4	-17.6	0.0	27.1	6.7	0.1
2004-12-09	02:57:06.37	ESO/VLT	NACO	Ks	-354.1	82.0	5.4	5.6	27.1	5.3	0.1
2004-12-10	02:43:19.05	ESO/VLT	NACO	Ks	-358.8	80.1	5.3	6.1	27.1	3.7	0.0
2004-12-14	02:46:59.11	ESO/VLT	NACO	Ks	-393.3	41.3	-21.8	-22.2	27.1	4.9	0.2
2004-12-14	03:23:21.02	ESO/VLT	NACO	Ks	-358.1	67.4	13.4	3.9	27.1	4.5	0.2
2004-12-20	01:11:00.37	ESO/VLT	NACO	Ks	-350.9	46.2	2.2	-0.4	27.1	4.2	0.0
2004-12-20	03:57:24.97	ESO/VLT	NACO	Ks	-348.9	54.1	3.5	7.9	27.1	4.2	0.1

Table A.5: Astrometry of (4674) Pauling's satellite S/2004 (4674) 1, see Table A.1 for a description of the columns.

Date	UTC	Tel.	Cam.	Filter	X_o (mas)	Y_o (mas)	X_{o-c} (mas)	Y_{o-c} (mas)	σ (mas)	ΔM (mag)	δM (mag)
2004-03-04	05:30:40.08	ESO-VLT	NACO	Ks	-302.8	249.1	0.2	5.4	27.1	3.6	0.2
2004-03-04	05:41:18.31	ESO-VLT	NACO	H	-311.4	248.3	-8.3	4.6	13.3	4.3	0.2
2004-03-04	05:53:20.04	ESO-VLT	NACO	J	-307.9	240.3	-4.7	-3.3	13.3	4.8	0.7
2004-03-04	07:11:14.62	ESO-VLT	NACO	Ks	-309.0	242.8	-5.1	-0.7	27.1	3.4	0.3
2005-09-10	11:42:01.13	Keck II	NIRC2	Kp	222.7	-55.3	-1.1	14.0	10.0	2.9	0.0
2007-05-28	10:15:45.14	Keck II	NIRC2	Kp	-404.0	-73.0	-7.2	-11.7	10.0	5.4	0.6
2012-06-22	07:59:36.29	Keck II	NIRC2	Kp	-345.4	-70.9	5.1	6.3	10.0	2.7	0.0
2012-06-27	08:57:47.33	Keck II	NIRC2	Kp	-380.3	-58.1	-0.7	4.5	10.0	3.0	0.0
2012-06-27	09:05:35.66	Keck II	NIRC2	H	-380.4	-58.2	-0.7	4.4	10.0	3.1	0.0
2012-06-27	09:13:56.33	Keck II	NIRC2	J	-381.2	-59.5	-1.5	3.0	10.0	3.4	0.1
2012-06-27	10:35:11.14	Keck II	NIRC2	Kp	-377.9	-57.4	2.0	4.9	10.0	3.1	0.0
2012-07-15	07:36:06.96	Keck II	NIRC2	Kp	-323.0	9.4	1.7	-1.0	10.0	2.9	0.0
2012-07-15	07:39:22.23	Keck II	NIRC2	H	-323.2	9.1	1.5	-1.3	10.0	3.0	0.0
2012-07-15	09:32:42.36	Keck II	NIRC2	Kp	-320.0	9.2	4.0	-1.5	10.0	3.0	0.0

Table A.6: Astrometry of (17246) Christophedumas' satellite S/2004 (17246) 1, see Table A.1 for a description of the columns.

Date	UTC	Tel.	Cam.	Filter	X_o (mas)	Y_o (mas)	X_{o-c} (mas)	Y_{o-c} (mas)	σ (mas)	ΔM (mag)	δM (mag)
2004-01-14	10:05:10.00	HST	ACS	F606W	-181.4	18.3	0.3	0.4	3.0	2.0	0.0
2005-05-18	01:24:23.00	HST	ACS	F775W	108.7	4.0	-0.2	0.2	3.0	2.0	5.8
2005-05-25	12:31:13.00	HST	ACS	F775W	-12.6	68.0	0.3	0.1	3.0	3.6	0.1
2005-06-25	03:57:43.00	HST	ACS	F775W	-79.3	-21.7	0.1	0.0	3.0	1.9	0.1

Table A.7: Astrometry of (22899) Alconrad's satellite Juliekaibarreto, see Table A.1 for a description of the columns.

Date	UTC	Tel.	Cam.	Filter	X_o (mas)	Y_o (mas)	X_{o-c} (mas)	Y_{o-c} (mas)	σ (mas)	ΔM (mag)	δM (mag)
2003-07-26	03:45:47.00	HST	ACS	F606W	-119.2	-79.5	0.6	0.3	3.0	2.3	0.0
2004-11-01	09:14:22.00	HST	ACS	F775W	67.1	-55.5	1.4	-3.2	3.0	2.8	0.1
2004-11-13	23:38:58.00	HST	ACS	F775W	-91.6	34.9	-0.3	0.4	3.0	2.4	0.0
2004-12-21	10:21:48.00	HST	ACS	F775W	124.5	-61.5	0.2	0.1	3.0	2.6	0.0
2004-12-27	11:53:24.00	HST	ACS	F775W	90.8	-42.9	-1.2	2.7	3.0	2.4	0.1

Appendix B: Infrared photometry

Tables B.1 and B.2 contain infrared photometry measurements from Spitzer observations of (17246) Christophedumas and (22899) Alconrad, respectively.

Table B.1: Spitzer measurements for (17246) Christophedumas.

Telescope	Observation Mid-Time	r (au)	Δ (au)	α(deg)	
Spitzer	2005-Aug-22 16:38	2.7815	2.4091	-21.2	
	Instrument/Band	λ (μm)	flux density (mJy)	Meas. unc. (mJy)	Total unc. (mJy)
	IRAC1	0.0410	0.0016	0.0020	
	IRAC2	0.0471	0.0019	0.0024	
	IRAC3	5.73	0.213	0.008	0.010
	IRAC4	7.87	1.810	0.012	0.056
WISE	2010-Mar-14 16:30	2.7835	2.5899	+20.9	
	Instrument/Band	λ (μm)	flux density (mJy)	Meas. unc. (mJy)	Total unc. (mJy)
	W3	11.1	6.2	-	0.6
	W4	22.6	17.8	-	4.1

Table B.2: Spitzer measurements for (22899) Alconrad.

Telescope	Observation Mid-Time	r (au)	Δ (au)	α(deg)	
Spitzer	2005-Dec-27 07:35	3.0524	2.8078	+19.3	
	Instrument/Band	λ (μm)	flux density (mJy)	Meas. unc. (mJy)	Total unc. (mJy)
	IRAC1	0.0255	0.0005	0.0009	
	IRAC2	0.0252	0.0007	0.0010	
	IRAC3	0.0943	0.0037	0.0047	0.005
	IRAC4	0.9275	0.0055	0.0284	0.028
WISE	2010-Mar-11 02:00	2.9137	2.6496	+19.8	
	Instrument/Band	λ (μm)	flux density (mJy)	Meas. unc. (mJy)	Total unc. (mJy)
	W3	11.1	6.09	-	0.58
	W4	22.6	16.96	-	1.14

Appendix C: NEATM fits

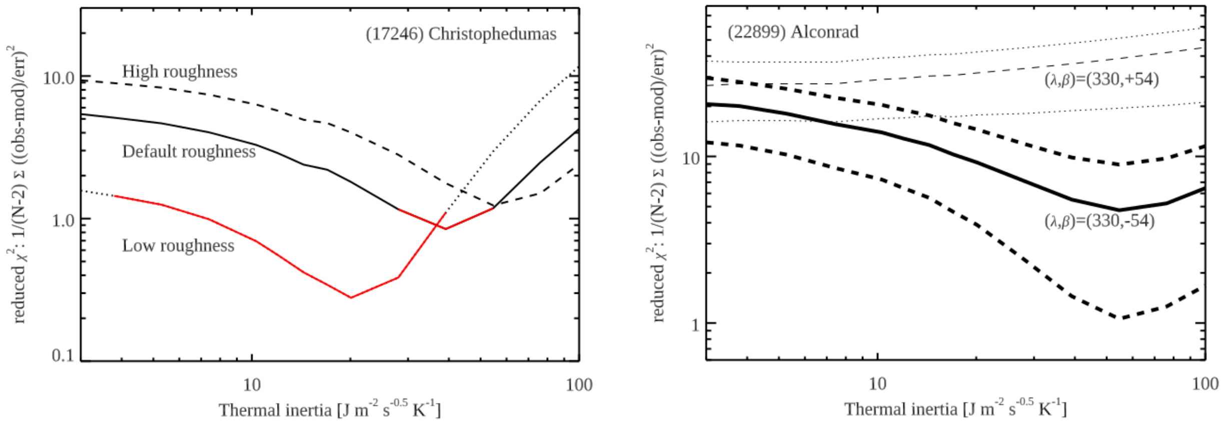

Fig. C.1: χ^2 curves from fitting TPM predictions to the WISE and Spitzer-IRAC data for asteroid (17246) Christophedumas (left) and (22899) Alconrad (right). For Christophedumas, three different TPM solutions are shown: assuming a low, (dotted line), intermediate (default value; see Müller & Lagerros (1998)), and high level (dashed line) of surface roughness. The red parts show acceptable TPM settings with possible thermal inertias in the range between 4 and 50 J m^{-2} s$^{-0.5}$ K^{-1}. For Alconrad, three different TPM solutions are shown for a prograde rotation of the primary (top 3 thin lines), and another three lines (thick dashed and solid lines) for the retrograde rotation case. Based on our radiometric study, the retrograde rotation is strongly favored, possibly with a thermal inertia in the 30-100 J m^{-2} s$^{-0.5}$ K^{-1} range. The retrograde rotation is in agreement with the retrograde orbit of the satellite.